
	<p style="text-align: center;">DIMITRI_v4.x ATBD Interband Vicarious Calibration over Sunlint</p>	<p>Reference: ARG_DIM_QA4EO-TN-004c Revision: 2.1 Date: 30/09/2019 Page: i</p>
---	--	--

DIMITRI Algorithm Theoretical Basis Document

Interband Vicarious Calibration over Sunlint




ESA contract: 4000114544/15/I-SBo
ARGANS Reference: ARG_DIM_QA4EO-TN-004c
Date: 30th September 2019
Version: 2.1

	DIMITRI_v4.x ATBD Interband Vicarious Calibration over Sunlint	Reference: ARG_DIM_QA4EO-TN-004c Revision: 2.1 Date: 30/09/2019 Page: ii
---	--	---

	NAME	AFFILIATION	CONTACT
Prepared by	B. Alhammoud	ARGANS Ltd, UK	balhammoud@argans.co.uk
Prepared by	J. Hedley	Numerical Optics Ltd, UK	j.d.hedley@envirocs.com
Reviewed by	J. Hedley Marc Bouvet	NOL ESTEC	j.d.hedley@envirocs.com Marc.Bouvet@esa.int
Approved by	Marc Bovet	ESTEC	Marc.Bouvet@esa.int

Acknowledgements

The Siro modelling included in Figure 8 and Figure 9: were produced Jukka Kujanpää of the Finnish Meteorological Institute in the context of the ESA project 'GEO-HR' AO/1-7084/12/NL/AF, and are reproduced from Hedley *et al.* (2013).


	DIMITRI_v4.x ATBD Interband Vicarious Calibration over Sunlint	Reference: ARG_DIM_QA4EO-TN-004c Revision: 2.1 Date: 30/09/2019 Page: iii
---	--	--

Version History

Version	Date	Main Changes
1.0	28/05/2014	<u>ATBD, ref: 003-013: MO-SCI-ARG-TN-004c</u> Edited to reflect the implementation in DIMITRI V3.0 onward
2.0	28/03/2019	The ATBD is updated to reflect the implementation in DIMITRI V4.3.1 onward. Mainly the implementation of the Hyperspectral LUTs “Ref: ARG_DIM_QA4EO_LUT_SUM” Including the Water leaving BRDF “Ref: ARG_DIM_QA4EO_WL_BRDF” And Atmospheric pressure adjustment “Ref: ARG_DIM_QA4EO_ATM”
2.1	30/09/2019	Overall the ATBD revision and added reference (Bouvet 2013)

TABLE OF CONTENTS

1	Introduction	1
1.1	Scope of this ATBD	1
1.2	DIMITRI	1
2	Interband Vicarious Calibration over Sunlint	6
2.1	Overview	6
2.2	Algorithm description.....	7
2.2.1	Oceanic sites	7
2.2.2	Data screening	7
2.2.3	Marine model.....	8
2.2.4	Atmospheric model.....	13
2.2.5	Calibration coefficient algorithm	18
3	Uncertainty analysis	22
3.1	Published error budget	22
3.2	Sensitivity analysis on DIMITRI data	22
3.2.1	Tentative random/systematic uncertainty breakdown.....	24
4	Presentation of the implementation in DIMITRI_v4.x making use of Hyperspectral LibradTran LUTs and Hydrolight version 5.2 mode	26
4.1	Radiative transfer Look up tables (LUT)	26
4.1.1	Format specification in DIMITRI	26
4.1.2	Atmospheric radiative transfer LUTs generation	29
4.1.3	Computational considerations.....	29
4.1.4	Details of the required tables	31
4.1.5	Details of LibRadtran parameterisation.....	34
4.1.6	Aerosol models	35
4.2	Auxiliary data for marine modelling.....	36
4.3	Output files generated by the glint intercalibration	38
4.4	DIMITRI modules/functions/architecture.....	38
4.5	HMI updates and User options	38
5	Results and implementation comparisons.....	41

	DIMITRI_v4.x ATBD Interband Vicarious Calibration over Sunlint	Reference: MO-SCI-ARG-TN-004c Revision: 2.1 Date: 30/09/2019 Page: v
---	--	---

5.1	DIMITRI implementation results for MERIS	41
5.2	DIMITRI implementation results for other sensors	47
6	Discussion and conclusion.....	50
7	References	51

List of Figures

Figure 1:	DIMITRI v4.x.y screenshot	3
Figure 2:	Example of TOA reflectance factors simulated in a viewing direction (solar zenith = 40, viewing zenith = 43.5, relative azimuth = 174) close to the exact specular direction, for all VEGETATION spectral bands and for three different values of wind speed (Hagolle <i>et al.</i> , 2004).	6
Figure 3:	Variation in f/Q with solar zenith angle (here θ_0) and chlorophyll concentration (0.03 to 3 mg m^{-3}). Reproduced from Moral and Gentili (1996).	11
Figure 4:	Comparison of the Morel and Maritorena (2001) reflectance model with Hydrolight New Case 1 model at a nadir solar-view geometry, $\theta_s = 0$, $\theta_v = 0$, and also a typical SPG solar-view geometry, $\theta_s = 50^\circ$, $\theta_v = 20^\circ$ and $\Delta\phi = 60^\circ$, with wind speed $u_{10} = 0.5 \text{ ms}^{-1}$. Four wavelengths are shown, as labelled. The Morel and Maritorena is applied as implemented in DIMITRI, with $f = 0.33$ and $Q = \pi$ i.e. $f/Q = 0.105$	12
Figure 5:	Comparison of f/Q from Morel and Gentili (1996) and the BRDF produced with the HydroLight New Case 1 model. HydroLight results at 440 nm are the blue and red lines, the Morel and Gentili results represent several wavelengths with 440 nm generally being one of the upper lines. Red lines are 'pure BRDF' values assuming light is incident from the solar direction only. Blue lines include the HydroLight sky radiance model for typical clear sky conditions.	13
Figure 6:	Effect of wavelength on Rayleigh optical thickness as direct values (top), and log-log values (bottom). Calculated according to Bodhaine <i>et al.</i> (1999) and method described in Section 3.	16
Figure 7	Tentative random (yellow)/bias(red) uncertainty breakdown of Sunlint vicarious method, based on MERIS vicarious coefficients at SPG. Blue uncertainty is from the sensitivity study of section 3.1.2.	25
Figure 8:	Example Rayleigh scattering results from Hedley <i>et al.</i> (2013) at 443 nm, from the MERIS atmospheric correction look-up tables and from Mystic and Siro in spherical shell vectorial mode. <i>Left side:</i> Rayleigh scattering with error bars showing ± 1 standard error on the mean for Mystic results. <i>Right side:</i> corresponding percentage difference between MERIS and Siro, and MERIS and Mystic. <i>Note:</i> both Mystic and Siro predict an error of only one third of a percent due to plane parallel versus spherical shell modelling at zero solar and	

zenith angles, hence this is not an explanation for the small deviations of 2 – 3% seen here. 31

Figure 9: TOA reflectance from diffuse transmission paths as a function of bottom boundary Lambertian albedo from Hedley *et al.* (2013). These results were calculated in scalar spherical shell Mystic with the MAR-99 aerosol model (MERIS aerosol no. 4) $\tau_a(550) = 0.83$, but the general conclusion of linearity with bottom reflectance will hold for plane parallel vectorial modelling. Error bars are ± 1 standard error on the mean, line is least squares linear fit. 33

Figure 10: Aerosol optical thickness from 440 to 900 nm for the implemented aerosol models MAR50, MAR99 and MC50. Tabulated values for MAR50 and MAR99 from the MERIS atmospheric correction algorithm are also shown as point data..... 36

Figure 11 The monthly variations of the Chl1 climatology *CHL1Climmonth* derived from the full period 1998-2012 over SPG-optimum for applying the Raleigh scattering methodology. The black error bar is the associated uncertainty which the *CHL1_uncertaintyClimmonth* and the grey error bar is the *CHL1_stddevClimmonth*.. 37

Figure 12: DIMITRI v4.x.y window for parameterising the glint vicarious calibration 40

Figure 13: Time-series of (top) band-6 and (bottom) band-13 from MERIS 3rd reprocessing glint intercalibration coefficients as ratios TOA-Sensor/TOA-Simulation (665 nm as reference) over SPG-OPTIMUM, Error bars are method’s uncertainty 43

Figure 14: Time-series of (top) band-6 and (bottom) band-13 from MERIS 3rd reprocessing glint intercalibration coefficients as ratios TOA-Sensor/TOA-Simulation (665 nm as reference) over SPG-OPTIMUM, Error bars are method’s uncertainty 46

Figure 15: Time-series of (top) band-1 and (bottom) band-3 from AATSR 3rd reprocessing glint intercalibration coefficients as ratios TOA-Sensor/TOA-Simulation (666 nm as reference) over SPG-OPTIMUM, Error bars are method’s uncertainty. 49

List of Tables

Table 1: Sensors and sites coordinates included in the DIMITRI v4.x.y database..... 3

Table 2: Uncertainty budget of DIMITRI glint vicarious intercalibration coefficients in %, decomposed by sources. (*) comes from Hagolle *et al.* (1999) 24

Table 3: RHOR_SENSOR.txt template for Rayleigh reflectance LUT (MERIS example) 26

Table 4: TAUA_SENSOR_AER.txt template for spectral dependence of aerosol optical thickness LUT at given AER model (MERIS example for MAR-99)..... 27

Table 5: TRA_DOWN_SENSOR_AER.txt template for downward total transmittance LUT at given AER model (MERIS example for MAR-99)..... 27

Table 6: TRA_UP_SENSOR_AER.txt template for upward total transmittance LUT at given AER model (PARASOL example for MAR-99) 27

Table 7: Structure of BRDF LUT for $L_w / E_d(0+)$, i.e. ρ_w/π 28

Table 8: Structure of Rayleigh Optical thickness vs wavelength following Bodhaine et al., 1999.
 29


Table 9: Structure of look-up tables for one aerosol model. 34

Table 9: Components used in OPAC aerosol models as implemented in libRadtran (Hess *et al.* 1998) 35

Table 11: MERIS 3rd reprocessing glint intercalibration coefficients over SPG, relative to 665 nm (AR₆₆₅: 0.977) 41

Table 12: MERIS 3rd reprocessing glint intercalibration coefficients over SIO-Optimum, relative to 665 nm 43

Table 13: AATSR 3rd reprocessing glint intercalibration coefficients over SPG, relative to 666 nm 47

	DIMITRI_v4.x ATBD Interband Vicarious Calibration over Sunglint	Reference: MO-SCI-ARG-TN-004c Revision: 2.1 Date: 30/09/2019 Page: 1
---	---	---

1 Introduction

1.1 Scope of this ATBD

Under ESA contract 4000114544/15/I-SBo (“QA4EO-DIMITRI Evolution”) DIMITRI v3.x.y has been merged with DIMITRI v4.2.4 and further developed into DIMITRI v4.x.y (v4.3.1 onward), in which both the Rayleigh scattering and Sun-glint interband calibration methodologies originally developed by ARGANS have been improved. The two corresponding ATBDs are:

Absolute vicarious calibration over Rayleigh Scattering;

Interband vicarious calibration over Sunglint

This ATBD document is concerned with describing the vicarious calibration over Sun-glint. The document:


- 1) Describes the principles of this method;
- 2) Describes the implementation in DIMITRI v4.x.y making use of Hyperspectral libRadtran LUTs;
- 3) Presents results of implementation, sensitivity analyses and uncertainty estimations;
- 4) Describes the updates made to DIMITRI Human Machine Interface (HMI) and how the user can use this methodology.

1.2 DIMITRI

The Database for Imaging Multi-Spectral Instruments and Tools for Radiometric Intercomparison (DIMITRI) is an open-source software offering users the capability of radiometric performance assessment of optical imagers. It is coupled to a database of L1b products from a number of optical medium resolution sensors.

DIMITRI offers a suite of tools for comparison of the L1b radiance and reflectance values originating from various medium resolution sensors over a number of radiometrically homogenous and stable sites (Table 1) at TOA level, within the 400nm – 4µm wavelength range. The database (available separately from the software) covers the period 2002 to present. DIMITRI’s interface enables radiometric intercomparisons between sensors or against simulated signals (over ocean and desert sites).

After extraction from L1b products, the DIMITRI database contains for each site the mean reflectance and standard deviation (and number of valid pixels in the defined region of interest, or ROI), the viewing and solar geometries and auxiliary and meteorology information where available (windspeed and direction, surface pressure, humidity and ozone concentration). Each observation is automatically assessed for cloud cover using automated algorithms making use of each sensors spectral coverage; manual cloud screening can also be visually performed using

	DIMITRI_v4.x ATBD Interband Vicarious Calibration over Sunlint	Reference: MO-SCI-ARG-TN-004c Revision: 2.1 Date: 30/09/2019 Page: 2
---	--	---

product quicklooks to flag misclassified observations. Other capabilities and functions include: product reader and data extraction routines, database status visualisation and instrument spectral response comparison tool.

DIMITRI v2.0 offered two methodologies for radiometric performance assessment:

1. **Radiometric intercomparison based on angular and temporal matching**, based on the methodology of Bouvet (2006) and Bouvet *et al* (2007): Concomitant observations made under similar geometry and within a defined temporal window are intercompared at similar spectral bands.
2. **Radiometric intercomparison of VEGETATION simulated and actual observations**, making use of the ability to combine timeseries from all sensors into one “super sensor” and fitting a 3-parameter BRDF model to all observations to simulate TOA spectra of VEGETATION-2 (Bouvet, 2011).

DIMITRI v3.x is evolved from DIMITRI v2.0 and has two additional methodologies (below) and an improved automated cloud screening and cloud screening tool. Moreover the second methodology if DIMITRI v2.0 above was replaced by the methodology described in (Bouvet 2014) allowing simulating the TOA signal over desert sites.

In parallel to DIMITRI v3.x development, a new version v4.0 was developed by MAGELLIUM including new radiometric comparison methodologies (over ocean and desert sites) and aiming at giving a sounder software basis (improving modularity). **DIMITRI v4.3.1** is evolved from the merging of DIMITRI v3.x.y and DIMITRI v4.0. Furthermore , two methodologies originally present in DIMITRI v3.x were improved:

1. **Absolute vicarious calibration over Rayleigh Scattering**, based on the methodology of Hagolle *et al* (1999) and Vermote *et al* (1992) and utilising open ocean observations, to simulate molecular scattering (Rayleigh) in the visible and comparing against *the observed* ρ_{toa} to derive a calibration gain coefficient;
2. **Interband vicarious calibration over sunglint**, based on the methodology of Hagolle *et al* (2004); similar to Rayleigh scattering approach but accounting for sunglint reflectance contribution;

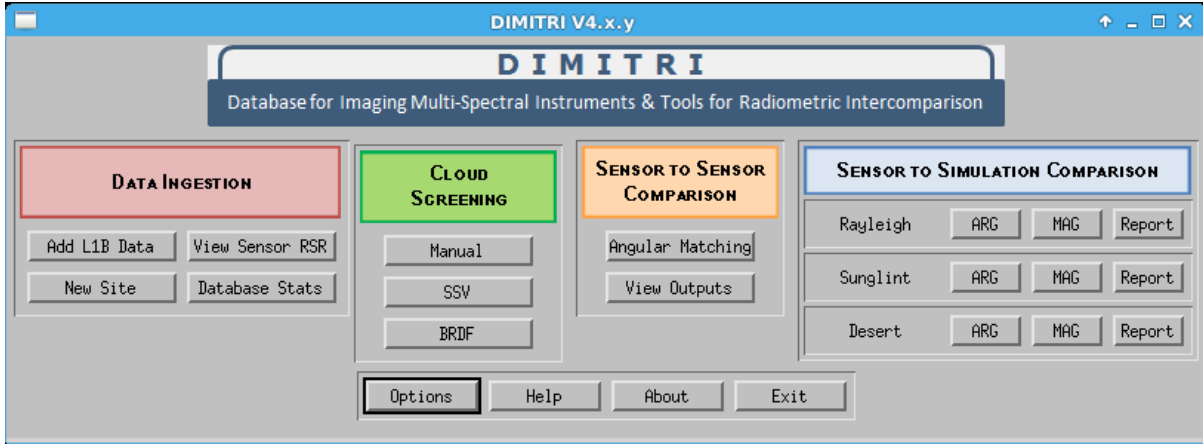



Figure 1: DIMITRI v4.x.y screenshot

Table 1: Sensors and sites coordinates included in the DIMITRI v4.x.y database.

Sensor	Data Supplier
AATSR	http://ats-mercids.eo.esa.int/merci/welcome.do
ATSR2	http://ats-mercids.eo.esa.int/merci/welcome.do
Landsat-8/OLI	https://landsat.usgs.gov/landsat-data-access
MERIS	http://mercisrv.eo.esa.int/merci/welcome.do http://www.odesa-info.eu/
MODIS-Aqua	http://ladsweb.nascom.nasa.gov/
PARASOL	http://polder.cnes.fr/en/index.htm
VEGETATION – 2*	http://www.vito-eodata.be
VIIRS	http://ladsweb.nascom.nasa.gov/

Sensor	Data Supplier
Sentinel-2A/MSI	https://scihub.copernicus.eu/
Sentinel-2B/MSI	
Sentinel-3A/OLCI	
Sentinel-3B/OLCI	
Sentinel-3A/SLSTR	
Sentinel-3B/SLSTR	

Site name	Site Type	North Latitude	South Latitude	East Longitude	West Longitude
AMAZON	Forest	1.33	1	-56.5	-57
DOME C	Ice	-74.9	-75.3	123.9	122.9
UYUNI	Salt	-20	-20.16	-67.45	-68.05
TUZ GOLU	Salt	38.8	38.7	33.4	33.25
ALGERIA-3	Desert	30.82	29.82	8.16	7.16
ALGERIA-5	Desert	31.52	30.52	2.73	1.73
LIBYA-1	Desert	24.92	23.92	13.85	12.85
LIBYA-4	Desert	29.05	28.05	23.89	22.89
MAURITANIA-1	Desert	19.9	18.9	-8.8	-9.8
MAURITANIA-2	Desert	21.35	20.35	-8.28	-9.28
BOUSSOLE	Ocean	43.45	43.25	8	7.8
SIO	Ocean	-30	-30.5	80.5	80
SPG	Ocean	-31	-31.5	-137	-137.5
SPG_OPTIMUM	Ocean	-24	-28	-118	-122
SIO_OPTIMUM	Ocean	-25	-29	80	76
NW_PACIFIC_OPTIMUM	Ocean	20	16	159	155
NE_PACIFIC_OPTIMUM	Ocean	20	16	-150	-154
NW_ATLANTIC_OPTIMUM	Ocean	25	21	-65	-69

	DIMITRI_v4.x ATBD Interband Vicarious Calibration over Sunlint	Reference: MO-SCI-ARG-TN-004c Revision: 2.1 Date: 30/09/2019 Page: 5
---	--	---

SW_ATLANTIC_OPTIMUM	Ocean	-12	-16	-22	-26
MEDSEA_OPTIMUM	Ocean	34	33	33	32
NE_AUSTRALIA_OPTIMUM	Ocean	-18	-20	155	153

DIMITRI_v2.0 and v3.0 are freely available (without the L1b database). DIMITRI_v2.0 is available following registration at www.argans.co.uk/dimitri. DIMITRI_v3.0 is a larger file (approx. 55GB) so is available upon request; ARGANS or ESA will make it available on an FTP server site.

DIMITRI_v4.x.y is still under development and validation, and will be released when fully validated.

2 Interband Vicarious Calibration over Sunlint

2.1 Overview

Interband calibration for Near Infra-red (NIR) and Shortwave Infrared (SWIR) bands can be computed by utilising the flat spectral slope of sun glint; the TOA reflectance can be simulated (e.g. Figure 2), similarly to the Rayleigh calibration methodology but taking into account the sunlint reflectance contribution. The magnitude of the sunlint reflectance is mainly dependent on the viewing and solar geometries and surface roughness (i.e. wind speed; Hagolle *et al.*, 2004). A 'reference' band (usually around 660 nm) is used to extrapolate the sunlint reflectance into the NIR/SWIR bands for comparison against the observed values. Pixels within the defined ROI are selected only if they fall within a defined cone of specular reflection; as the sunlint reflectance is spectrally flat (in the NIR/SWIR) (Hagolle *et al.* 2004).

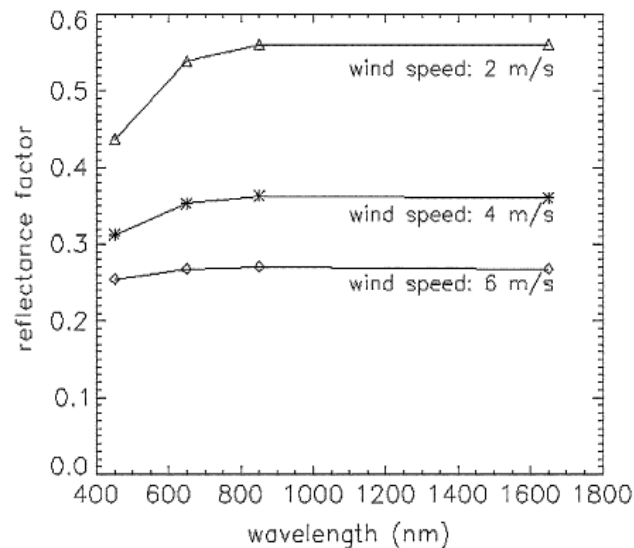



Figure 2: Example of TOA reflectance factors simulated in a viewing direction (solar zenith = 40, viewing zenith = 43.5, relative azimuth = 174) close to the exact specular direction, for all VEGETATION spectral bands and for three different values of wind speed (Hagolle *et al.*, 2004).

The sunlint method is often used together with Rayleigh method, see e.g., Nicolas *et al.* (2006) who apply it to SEVIRI. Sunlint (the Fresnel reflection of sunlight on the air-sea interface) can be used as a spectrally flat target to calibrate one spectral band according to another. For example, Nicolas *et al.* (2006) used the gain coefficient from Rayleigh scattering method of the visible (600 nm) band as a reference in order to calibrate the VNIR (800-1600 nm) bands. The sunlint signal ranged from 10 to 40 % of the maximum dynamic for each of the three bands.

	DIMITRI_v4.x ATBD Interband Vicarious Calibration over Sun glint	Reference: MO-SCI-ARG-TN-004c Revision: 2.1 Date: 30/09/2019 Page: 7
---	--	---

Závody *et al.* (1998) describe their implementation of the sunglint calibration method applied to the calibration of ATSR-2 1.6- μm channel using simultaneous measurements made in the 3.7- μm channel in the Sun glint. The theoretical model for their calibration is described in the following steps:

- finding the increase in radiance at 3.7 mm caused by sun glint,
- characterizing the atmosphere in the glint region,
- computing the effective reflectivity of the sea surface at 3.7 mm,
- finding the 1.6-mm surface reflectivity,
- calculating the 1.6-mm calibration coefficient.

Hagolle *et al.* (2004) conclude that despite the drawback of relying on the absolute calibration of a reference spectral band, this is one of the rare methods that can provide accurate calibration results for near-infrared spectral bands up to 1650 nm, without requiring costly in situ measurements simultaneously to the satellite overpass. The paper details the sunglint calibration method and its error budget, and gives the results obtained with the VEGETATION-2 instrument. The sunglint calibration method compares the measurements provided by VEGETATION-2 above sunglint, to an estimation of the top-of-atmosphere reflectance. The authors have evaluated error budget showing that if the reference spectral band uncertainty is below 3% (3 sigma), the calibration of NIR bands can be obtained with an uncertainty below 4% (3 sigma) at 850 nm and below 5% at 1650 nm (3 sigma). Apart from the reference spectral band calibration uncertainty, the main error contributors are the uncertainty on the water refraction index at 1650 nm, and the aerosol properties variability.


2.2 Algorithm description

The implemented DIMITRI sun glint calibration is based on the methodologies described in Hagolle *et al* (1999; 2004) and Nicolas *et al* (2006) and uses the specular reflection of the sun (i.e. sun glint) on the sea surface to transfer calibration from 565 nm (or close) band to the NIR bands (670 nm and above, relevant to each to sensor).

2.2.1 Oceanic sites

The Sun glint calibration methodology is applicable over stable oceanic regions, with low concentration of phytoplankton and sediment to reduce the impact of the marine signal in the red and near-infrared bands, and far from land to ensure purely maritime aerosol model.

2.2.2 Data screening

	DIMITRI_v4.x ATBD Interband Vicarious Calibration over Sunlint	Reference: MO-SCI-ARG-TN-004c Revision: 2.1 Date: 30/09/2019 Page: 8
---	--	---

Clear conditions must be chosen to avoid any signal contamination by clouds, haze or cloud shadows.

A low wind speed is required for both ensuring no presence of whitecaps; typically it is limited to 5 m/s.

In order to select only pixels impacted by the sunlint, the viewing direction must be within a cone around the specular direction. For a flat sea surface, the angle between viewing direction and specular direction is given by the backscattering angle:

$$\cos \theta_g = \cos \theta_s \cos \theta_v - \sin \theta_s \sin \theta_v \cos \Delta\phi \quad (1)$$


Where θ_s , θ_v and $\Delta\phi$ are respectively the sun zenith angle, view zenith angle and relative azimuth angle. To take into account wavy surface, a cone around $\theta_g=0^\circ$ is allowed, for instance of about 15° (default value proposed in DIMITRI).

Contrary to Hagolle *et al.* (1999) using PARASOL off-glint data, DIMITRI database contains a large set of sensors without multi-directional capability (e.g. MERIS, MODIS). This precludes computing the aerosol optical thickness from the radiometry. Therefore, as presented hereafter, a climatological value must be given by user for all measurements; default value proposed at 865 nm is 0.02, corresponding to Rayleigh scattering retrieval out of glint over SPG and SIO, as described in Barker *et al.* (2013). A test is conducted a-posteriori on the retrieved optical at 865 nm, after glint estimate: data are screened with a threshold of 0.02 between the climatological value and this retrieved estimate, so that only consistent inversions are kept.

2.2.3 Marine model

In DIMITRI versions prior to V4.3.1, the marine model follows Morel and Maritorena (2001), which is an update of Morel (1988) used in Hagolle *et al.* (1999). It provides an estimate of irradiance reflectance at null depth, $R(0^-)$, from 350 to 700 nm, as a function of chlorophyll concentration and sun zenith angle, but it does not take in account for the viewing geometry (c.f. neglecting the BRDF effects).

The simplest method to incorporate BRDF effects in L_w is to replace $\rho_w(\lambda)$ with a directionally dependent value $\rho_w(\lambda, \theta_s, \theta_v, \Delta\phi)$. Therefore implementing the water leaving BRDF in terms of $\rho_w(\lambda, \theta_s, \theta_v, \Delta\phi)$ will lead to a potential overestimate of the BRDF effect at TOA, because the assumption is that the total transmission is entirely direct transmission. In reality, atmospheric scattering redistributes a portion of the light and will 'blur out' the BRDF effect. Previous investigation has indicated that the libRadtran Mystic solver lacks the capability for directionally tabulating the radiance at BOA, as would be required to do this (Hedley 2017). Since the

	DIMITRI_v4.x ATBD Interband Vicarious Calibration over Sunlint	Reference: MO-SCI-ARG-TN-004c Revision: 2.1 Date: 30/09/2019 Page: 9
---	--	---

reflectance is dependent on the chlorophyll concentration, the actual requirement is for a five parameter function, $\rho_w(\lambda, \theta_s, \theta_v, \Delta\phi, [chl])$, where $[chl]$ is the chlorophyll concentration in mg m^{-3} . For the implementation in DIMITRI, this function has been tabulated as a five dimensional look-up table (LUT), more details in (Hedley 2017).

Since HydroLight is now used to generate the BRDF LUT, where it calculates by exact physical methods based on the water absorption and volume scattering function, and provides water leaving radiance (L_w) directly, as did the Monte Carlo model used by Morel and Gentili.

The basis of the current DIMITRI water leaving reflectance model lies in Morel (1988) where it is stated by reference to work by Gordon and Kirk that subsurface irradiance reflectance, $R(0^-)$ is to a good approximation expressed by:

$$R = 0.33 \frac{b_b}{a} \quad (2)$$

At that time it was suggested that the factor 0.33, which later became denoted f , varied only slightly due to illumination conditions, supported by the paper of Kirk (1981). The paper on which the current DIMITRI reflectance model is based (Morel and Maritorena 2001) is concerned primarily with b_b/a component of this expression and says relatively little about f , which in DIMITRI is fixed at 0.33 as above.


In order to translate subsurface irradiance reflectance $R(0^-)$ to above surface reflectance additional terms are required, and this results in the expression as appears in the DIMITRI Rayleigh calibration ATBD

$$\rho_w(\lambda) = \pi \frac{\mathfrak{R}}{Q} R(0^-) \quad (3)$$

Where:

\mathfrak{R} is the term accounting for all the reflection and refraction effects, with averaged value of 0.5287 for moderate wind speed (see Appendix D of Morel and Gentili, 1996); and

Q which can be interpreted as the ratio of the upwelling radiance to the upward planar irradiance just below the surface, i.e. $Q = L_u(0^-) / E_u(0^-)$. Q is a measure of the anisotropy of the upwelling radiance below the surface, in DIMITRI it is fixed as π which implies isotropic upwelling radiance

	DIMITRI_v4.x ATBD Interband Vicarious Calibration over Sunlint	Reference: MO-SCI-ARG-TN-004c Revision: 2.1 Date: 30/09/2019 Page: 10
---	--	--

(radiance equal in all directions over the upward hemisphere).;. The satellite sensor of course does not see the result of the irradiance reflectance of the surface, it primarily sees the radiance reflected in a particular direction. So although the application of π in a sense implies isotropic upward radiance above the surface this π term isn't relevant as part of the BRDF.

Combining equations 2 and 3 above leads to the expression presented in Morel and Gentili (1996), which is the full expression of what is required for DIMITRI in the terms of the parameters discussed:

$$L_w(\theta, \theta_0, \Delta\phi) = E_d(0^+) \mathfrak{R}(\theta) \frac{f}{Q} \frac{b_b}{a} \quad (4)$$

Multiplying the output of this equation (L_w) by π gives ρ_w . The terms f and Q are dependent on solar-view geometry although this dependence is not shown above. In Morel and Gentili (1996) f is considered primarily dependent solar zenith, θ_s , while Q is potentially dependent on the full solar-view geometry expressed by θ_s , θ_v and $\Delta\phi$. The key point is that the BRDF properties are entirely captured by $\mathfrak{R} \times f/Q$, and for θ_v less than 60° primarily by f/Q because \mathfrak{R} is almost constant. While f and Q individually vary with solar zenith angle to quite a large degree, their individual variations cancel out to some extent so that the overall effect on water leaving BRDF is reduced (Figure 3)

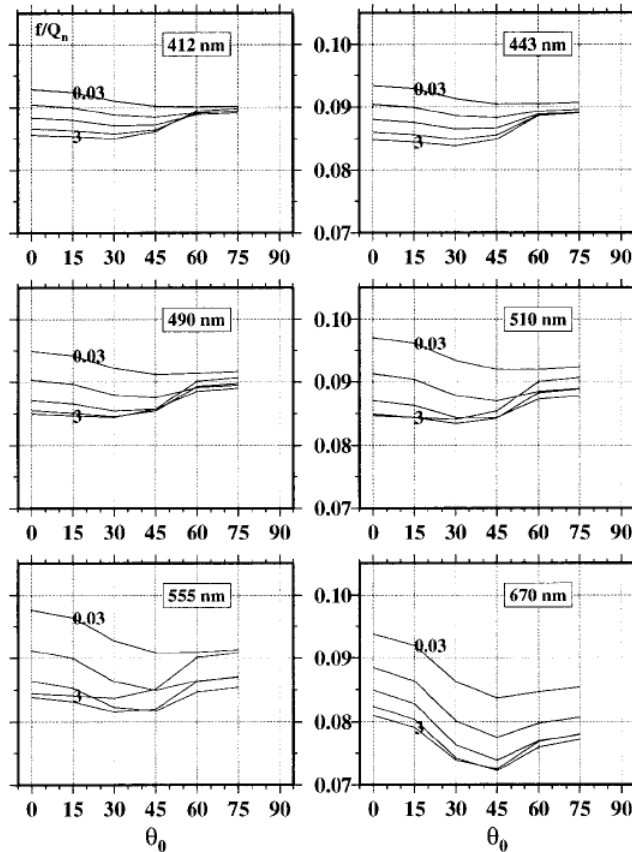


Figure 3: Variation in f/Q with solar zenith angle (here θ_0) and chlorophyll concentration (0.03 to 3 mg m^{-3}).
Reproduced from Morel and Gentili (1996).

In order to replicate the water leaving BRDF presented by Morel and Gentili (1996) and tabulate it in a form that can be used in DIMITRI, the software HydroLight version 5.2 has been used (Mobley and Sundman 2013).

The model provides close agreement to both the current DIMITRI reflectance function, based on Morel and Maritorena (2001), and the BRDF effects shown in Morel and Gentili (1996) (Figure 4). The final structure of the LUT is given in (Table 7; see Hedley 2017). Note the tabulated values are $L_w/E_d(0+)$ so must be multiplied by π to give ρ_w .

The comparison between HydroLight and Morel and Gentili f/Q results (Figure 5) is good for θ_v less than 60° . Note Figure 5 is presented in terms of the sub-surface refracted solar zenith angle θ' , so $\theta' = 40^\circ$ is $\theta_v \approx 60^\circ$. Recalling that f/Q encapsulates the BRDF effect, Figure 5 shows that the HydroLight BRDF is in generally good agreement with the results of Morel and Gentili. The difference seen in Figure 5 at view angles greater than 60° is due to taking a fixed value of \mathfrak{R} . The HydroLight results contain the 'true' view-dependent \mathfrak{R} and are correct.

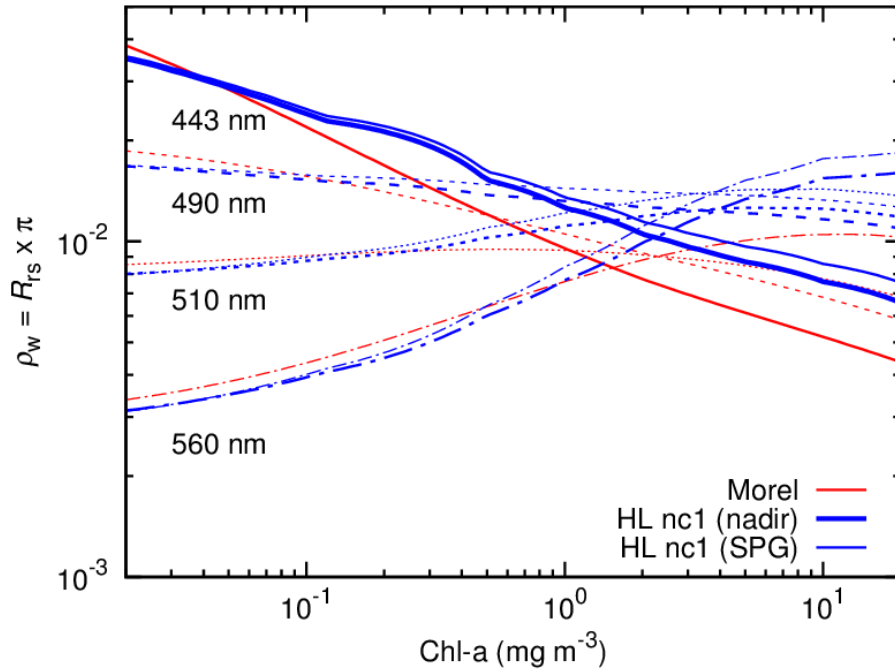
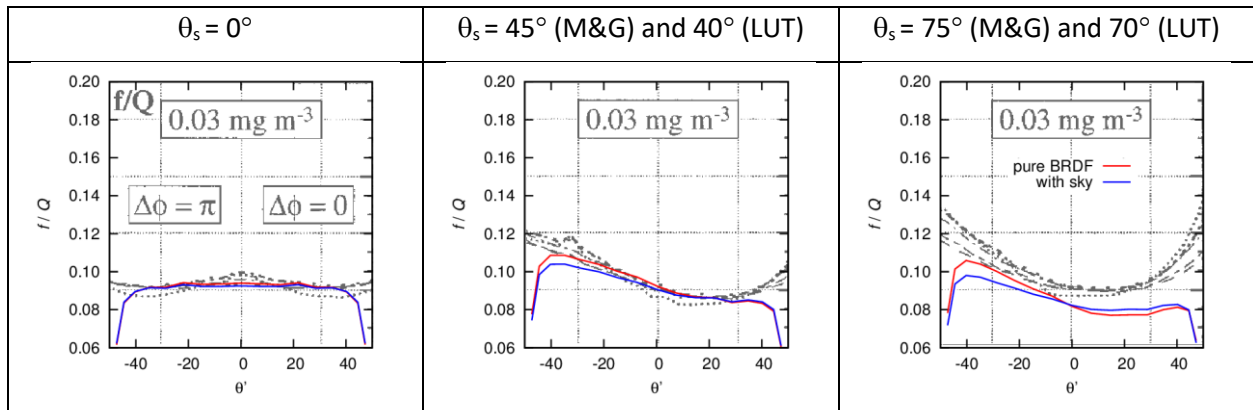


Figure 4: Comparison of the Morel and Maritorena (2001) reflectance model with Hydrolight New Case 1 model at a nadir solar-view geometry, $\theta_s = 0$, $\theta_v = 0$, and also a typical SPG solar-view geometry, $\theta_s = 50^\circ$, $\theta_v = 20^\circ$ and $\Delta\phi = 60^\circ$, with wind speed $u_{10} = 0.5 \text{ ms}^{-1}$. The Morel and Maritorena is applied as implemented in DIMITRI, with $f = 0.33$ and $Q = \pi$ i.e. $f/Q = 0.105$.



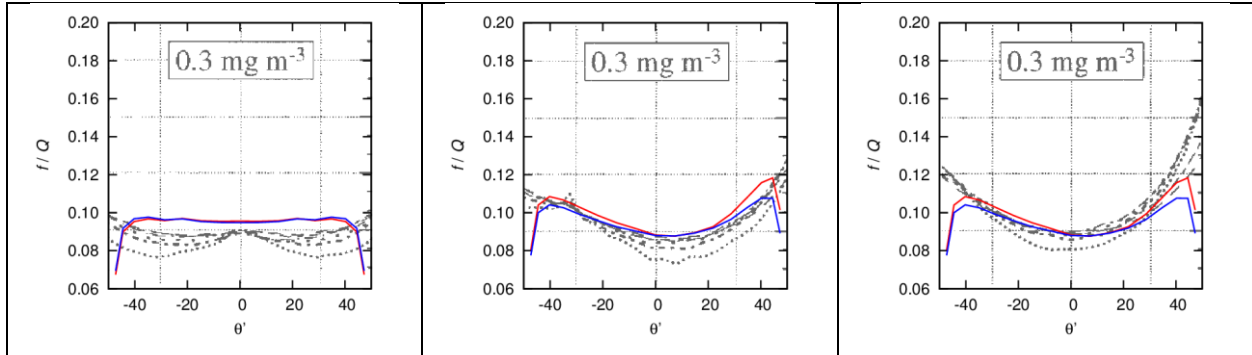


Figure 5: Comparison of f/Q from Morel and Gentili (1996) and the BRDF produced with the HydroLight New Case 1 model. HydroLight results at 440 nm are the blue and red lines, the Morel and Gentili results represent several wavelengths with 440 nm generally being one of the upper lines. Red lines are ‘pure BRDF’ values assuming light is incident from the solar direction only. Blue lines include the HydroLight sky radiance model for typical clear sky conditions.

2.2.4 Atmospheric model

The total TOA signal can be written as

$$\rho_{TOA}(\lambda) = t_{gas}(\lambda)(\rho_{path}(\lambda) + t_{down}(\lambda) * t_{up}(\lambda) * \rho_w(\lambda) + T_{down}(\lambda) * T_{up}(\lambda)\rho_G) \quad (5)$$

Where:

t_{gas} is the transmittance (downward and upward) due to absorbing gas as O₃, O₂ and H₂O

ρ_{path} is the atmospheric reflectance due to Rayleigh and aerosols and their multiple-scattering interaction

t_{down} and t_{up} are respectively the downward and upward total transmittance (i.e. direct + diffuse) due to Rayleigh and aerosol


ρ_w is the marine signal already described

T_{down} and T_{up} are the downward and upward direct transmittances

ρ_G is the sun glint reflectance at sea level.

The calibrated bands in the visible are only impacted by ozone. Hence the gaseous transmittance is computed by Beer’s law:

$$t_{O_3}(\lambda) = e^{-\tau_{O_3}(\lambda)*O_3*M} \quad (6)$$

	DIMITRI_v4.x ATBD Interband Vicarious Calibration over Sunlint	Reference: MO-SCI-ARG-TN-004c Revision: 2.1 Date: 30/09/2019 Page: 14
---	--	--

Where:

O_3 is the ozone concentration of actual measurement

τ_{O_3} the ozone optical thickness at a standard concentration (already provided in DIMITRI auxiliary data)

M the air mass fraction.

In the near-infra red, the impact of water vapour is lower than 0.2% at 865 nm and less at other bands except 709 nm. The impact of O_2 is of about 0.1% at 779 nm. Because DIMITRI currently does not contains auxiliary data about those gases, their transmittance is assumed to be unity (this will be included in error budget), and absorption bands (like 708 nm, 761 nm, 900 nm) are excluded of the vicarious calibration by a array of indices common to all DIMITRI wavelengths

The sun glint reflectance ρ_G is taken from the isotropic model of Cox and Munk (1954) as a function of wind speed modulus and geometry:

$$\rho_G = CM54(w_m, \theta_s, \theta_v, \Delta\varphi, \lambda) \quad (7)$$

The spectral dependence is due to the Fresnel coefficient, computed as a function of water refraction index; for a salinity of 35 PSU and temperature of 12°C the spectral variation of this index yields to a variation in the Fresnel coefficient (hence in the glint reflectance) of -2% from 560 to 865 nm, which is worth to taking into account.

Direct transmittance can be approximated by:

$$T_{down}(\lambda) * T_{up}(\lambda) = e^{-(\tau_R(\lambda) + \tau_a(\lambda)) * M} \quad (8)$$

With τ_R being the Rayleigh optical thickness at standard pressure computed following Bodhaine et al. 1999 (detailed below) and τ_a the aerosol optical thickness, assumed to be known at a reference band (865 nm).

The path reflectance and total transmittance are computed by radiative transfer simulations (see hereafter) for a set of aerosol models and optical thicknesses, and stored in Look-up tables (LUT). Aerosols models must be representative of the calibration zone; marine models of Shettle and

Fenn (1974) are here chosen for several relative humidity. Other more complex models may also be used for sensitivity study.

The aerosol optical thickness retrieved from a direct LUTs interpolation. Note that the AOT LUT is the result of direct calculation from the aerosol model and does not contain Monte Carlo noise unlike the other LUTs (see Hedley 2018 “ATBD-LUTs-SUM”).

$$\tau_a(\lambda) \rightarrow LUTs\ Linear_interpolation(\lambda, w_m, \theta_s, \theta_v, \Delta\varphi) \quad (9)$$

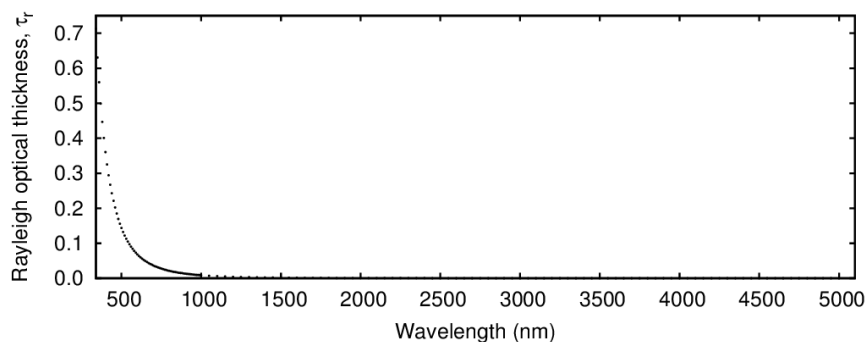
Radiative transfer simulations are only tabulated for the unique standard atmospheric pressure. Because the actual measurements are under different pressures, P , generally systematically higher due to clear sky condition, a correction on ρ_{path} and $t_{down} * t_{up}$ and $T_{down} * T_{up}$ are necessary and done following (Bodhaine et al. 1999; Hedley 2018 ATBD-Pressure correction).

The pressure correction algorithm makes direct use of the hyperspectral HS147 LUTs for atmospheric reflectance (ρ_{path}) and for upward and downward transmission (t_u and t_d).

In the pressure correction it is assumed that the wavelength at the band centres is representative of the full band width, this is necessary because it is not feasible to pre-calculate corrections resampled to the band RSRs. Any error is likely to be negligible for narrow bands such as MERIS or OLCI, and for wider bands, such as Sentinel 2, the issue of neglecting within-band spectral calculations is a limitation for in DIMITRI in general. In the reference code (see below) all calculations are performed hyperspectrally and convolved to band RSRs at the end.

1. Initialisation

Construct a table of wavelength, λ , and Rayleigh optical thickness, τ_r , according to standard LUT. i.e. columns 1 and 2 from Hedley 2018 ATBD-Pressure correction. The purpose of this table is to allow an interpolated log-log look-up to give wavelength as a function of Rayleigh optical thickness (Figure 6) therefore it may be most efficient to tabulate the natural log of λ and τ_r .



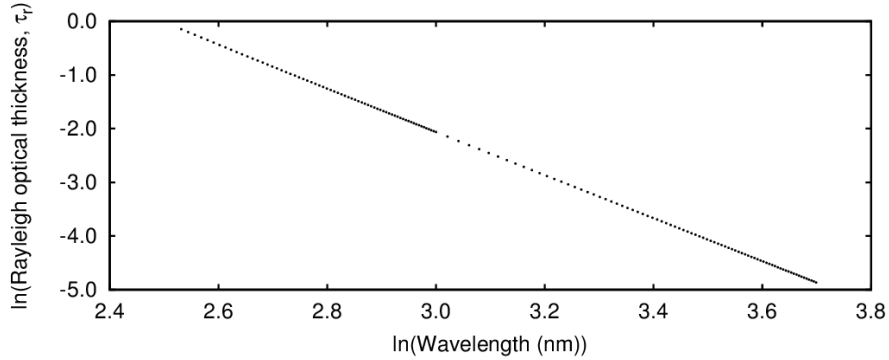


Figure 6: Effect of wavelength on Rayleigh optical thickness as direct values (top), and log-log values (bottom). Calculated according to Bodhaine et al. (1999) and method described in Section 3.

Then for each image subset to be processed:

2. Correction of ρ_{path}

At any point at which the band $\rho_{\text{path}}(\text{band})$ is read from the RSR resampled LUT:

2.1 Read the corresponding $\rho_r(\lambda)$ from the hyperspectral LUT, that is according to the same solar-view geometry and wind speed. Where λ is the band centre and $\rho_r(\lambda)$ is value obtained when the aerosol optical thickness $\tau(550)$ is set to zero.


2.2 Calculate the Rayleigh optical thickness, τ_r , for the pressure, latitude and CO_2 corresponding to the image subset following Bodhaine et al. 1999 (detailed in Hedley 2018 ATBD).

2.3 Find by log-log interpolation of the table prepared in the initialisation (Figure 6) the wavelength at which this τ_r occurs, denoted λ_{adj} .

2.4 Read $\rho_{\text{path}}(\lambda_{\text{adj}})$ and $\rho_r(\lambda_{\text{adj}})$ from the hyperspectral LUT.

2.5 Correct $\rho_{\text{path}}(\text{band})$ by applying the following calculation, which applies the change in Rayleigh reflectance between the standard wavelength, λ , and the wavelength that has the desired Rayleigh optical thickness, λ_{adj} .

$$\rho_{\text{path}}(\lambda) \rightarrow \rho_{\text{path}}(\lambda) + \rho_r(\lambda_{\text{adj}}) - \rho_r(\lambda) \quad (10)$$

	DIMITRI_v4.x ATBD Interband Vicarious Calibration over Sunlint	Reference: MO-SCI-ARG-TN-004c Revision: 2.1 Date: 30/09/2019 Page: 17
---	--	--

3. Correction of total transmission $t_u \times t_d$

The band transmissions $t_u(\text{band})$ and $t_d(\text{band})$ must similarly be corrected for the change in Rayleigh optical thickness, in practice these are used only as their product, total transmission $t_u(\text{band}) \times t_d(\text{band})$, and are read from the RSR resampled LUTs at the same time as $\rho_{\text{path}}(\text{band})$. Steps 2.2 and 2.3 above, estimation of λ_{adj} , are common with the ρ_{path} correction, so at any point after step 2.3 do this:

3.1 Read the corresponding $t_{ur}(\lambda)$ and $t_{dr}(\lambda)$ from the hyperspectral LUT, as a function of solar-view geometry. Where λ is the band centre and $t_{ur}(\lambda)$ and $t_{dr}(\lambda)$ are the values obtained when the aerosol optical thickness $\tau(550)$ is set to zero.

3.2 Read $t_{ur}(\lambda_{\text{adj}})$ and $t_{dr}(\lambda_{\text{adj}})$ from the hyperspectral LUT.

3.3 Correct $t_u(\text{band}) \times t_d(\text{band})$ by applying the following calculation, which applies the change in transmission between the standard wavelength, λ , and the wavelength that has the desired Rayleigh optical thickness, λ_{adj} . Note the effect here is assumed multiplicative, whereas for ρ_{path} it was considered additive.

$$t_u(\lambda) \times t_d(\lambda) \rightarrow [t_u(\lambda) \times t_d(\lambda)] \times [t_{ur}(\lambda_{\text{adj}}) \times t_{dr}(\lambda_{\text{adj}})] / [t_{ur}(\lambda) \times t_{dr}(\lambda)] \quad (11)$$

4. Correction of total transmission $T_u \times T_d$


Where direct transmission occurs it can be corrected by noting that the component of the direct transmission due to Rayleigh scattering is proportional to Rayleigh optical thickness and fully decoupled from the aerosol contribution. Direct transmission is losses to a beam which occur after a single scattering event. Direct transmission due to Rayleigh in the upward or downward path is

$$T(\lambda) = \exp[-M \times \tau_r(\lambda)] \quad (12)$$

where M is the air mass, i.e. relative path length, for the upward or downward path, $M = 1 / \cos\theta$.

The correction for $T_u(\text{band})$ and $T_d(\text{band})$ is performed by dividing through by the transmission due to Rayleigh optical thickness at the band centre (removing the 'standard' Rayleigh transmission) and then multiplying by the transmission with the desired Rayleigh optical thickness $\tau_r(\lambda_{\text{adj}})$. For downward transmission:

$$T_d(\lambda) \rightarrow T_d(\lambda) \times \exp[M_d \times \tau_r(\lambda) - M_d \times \tau_r(\lambda_{\text{adj}})] \quad (13)$$

	DIMITRI_v4.x ATBD Interband Vicarious Calibration over Sunlint	Reference: MO-SCI-ARG-TN-004c Revision: 2.1 Date: 30/09/2019 Page: 18
---	--	--

For the upward transmission the expression is the same, but replacing M_d with the upward path length M_u . The correction relies only on the tabulated reference Rayleigh thicknesses (Figure 6) and the Rayleigh thickness function (See above). Note that the hyperspectral LUTs are not used in the direct transmission correction.

5. Aerosol optical thickness determination

The aerosol thickness determination is performed by an interpolation of the look-up on the band LUT $\rho_{\text{path}}(\text{band})$ values at the reference band (e.g. 865 nm). Pressure correction therefore simply requires each of those values to be corrected as described above before the interpolated look-up. The total transmission correction is not required in the aerosol thickness determination.


2.2.5 Calibration coefficient algorithm

Glint calibration starts from a reference band λ_{ref} in the red assumed to be well-calibrated and intercalibrates other bands towards the near-infrared region. Hagolle *et al.* (1999) starts from 565 nm on PARASOL while Fougnie *et al.* (2012) uses 620 nm. The 665 nm band is also interesting for minimising ozone absorption, and can also be calibrated by the Rayleigh method. In DIMITRI this reference band is left to user choice. From a-priori knowledge of aerosol optical thickness τ_{865} and aerosol model, this reference band provides the sea surface state (i.e. wind speed) through Cox and Munk (1954). This model can be efficiently inversed alone by non-linear technique (here Newton method, at least when a solution exists), but we must consider that atmospheric path reflectance also depends in a lesser extent on wind speed. An iterative procedure is thus deployed to compute a wind speed that perfectly allows modelling the signal at reference band; three iterations are enough for converging on all cases encountered in DIMITRI, starting from the auxiliary wind speed. At the end of the algorithm, a check is done to inverse aerosol optical thickness and only pixels with sufficiently close value to the initial guess are kept.

The algorithm consists of the following steps, repeated for all bands, λ :

1. Correct the TOA signal at λ_{ref} for ozone:

$$\rho_{TOA}^{O_3}(\lambda_{ref}) = \rho_{TOA}(\lambda_{ref}) / t_{O_3}(\lambda_{ref}) \quad (14)$$

	DIMITRI_v4.x ATBD Interband Vicarious Calibration over Sunlint	Reference: MO-SCI-ARG-TN-004c Revision: 2.1 Date: 30/09/2019 Page: 19
---	--	--

2. Given a chlorophyll concentration and solar-view geometry, compute marine reflectance at band λ_{ref} from Look-up tables using Hydrolight version5.2 model (Mobley and Sundman 2013) :

$$\pi \times \text{linear interpolated lookup } (\lambda, \theta_s, \theta_v, \Delta\phi, [\text{chl}]) \rightarrow \rho_w(\lambda_{ref}) \quad (15)$$

3. Propagate aerosol optical thickness τ_{865} at band λ_{ref} through tabulated spectral dependence for the given aerosol model:

$$\tau_{865} \xrightarrow{LUT\ aer} \tau_a(\lambda_{ref}) \quad (16)$$

4. Compute Rayleigh optical thickness as a function of wavelength, pressure, latitude, and CO₂ concentration, in a way that is consistent with Bodhaine et al. (1999)

$$\tau_r(\lambda) = \sigma \frac{PA}{mag} \quad (17)$$

5. Start loop for wind speed inversion:

5.1 Compute total path radiance (Rayleigh + aerosol) at band λ_{ref} and correct for pressure as above (10):

$$\tau_a(\lambda_{ref}) \xrightarrow{LUT\ aer} \rho_{path}(\lambda_{ref})_{|P_{std}} \quad (18)$$


$$\rho_{path}(\lambda_{ref})_{|P} = \rho_{path}(\lambda_{ref})_{|P_{std}} + \rho_r(\lambda_{adj}) - \rho_r(\lambda) \quad (19)$$

5.2 Compute downward and upward total transmittances (direct + diffuse), accounting for Rayleigh and aerosol, at band λ_{ref} , and correct for pressure as above (11):

$$\tau_a(\lambda_{ref}) \xrightarrow{LUT\ aer} t_{down}(\lambda_{ref})_{|P_{std}} = \{t_{down}\}(\lambda_{ref}, \tau_\lambda, w_m, \theta_s) \quad (20)$$

$$\tau_a(\lambda_{ref}) \xrightarrow{LUT\ aer} t_{up}(\lambda_{ref})_{|P_{std}} = \{t_{up}\}(\lambda_{ref}, \tau_\lambda, \theta_v) \quad (21)$$

$$t_{down}(\lambda_{ref}) * t_{up}(\lambda_{ref})_{|P} = [t_{down}(\lambda_{ref}) * t_{up}(\lambda_{ref})_{|P_{std}} * t_{dr}(\lambda_{adj}) *$$

	DIMITRI_v4.x ATBD Interband Vicarious Calibration over Sunlint	Reference: MO-SCI-ARG-TN-004c Revision: 2.1 Date: 30/09/2019 Page: 20
---	--	--

$$t_{ur}(\lambda_{adj}) / t_{dr}(\lambda) * t_{ur}(\lambda) \quad (22)$$

5.3 Compute the glint reflectance:

$$\rho_G(\lambda_{ref}) = \frac{\rho_{TOA}^{oz}(\lambda_{ref}) - \rho_{path}(\lambda_{ref})_{|P} - t_{down}(\lambda_{ref}) * t_{up}(\lambda_{ref})_{|P} * \rho_w(\lambda_{ref})}{T_{down}(\lambda_{ref}) * T_{up}(\lambda_{ref})} \quad (23)$$

5.4 Inverse wind speed by Newton non-linear scheme:

Find w_m such that:

$$\rho_G(\lambda_{ref}) = CM54(w_m, \theta_s, \theta_v, \Delta\varphi, \lambda_{ref}) \quad (24)$$

6. Redo steps 1 to 4 at band λ with retrieved w_m and ρ_G and construct theoretical TOA signal:

$$\rho_{TOA}^{theo}(\lambda) = \rho_{path}(\lambda)_{|P} + t_{down}(\lambda) * t_{up}(\lambda)_{|P} * \rho_w(\lambda) + T_{down}(\lambda) * T_{up}(\lambda) \rho_G \quad (25)$$

Where the spectral variation of $\rho_G(\lambda)$ is only due to Fresnel coefficient.

7. When $\lambda = 865$ nm, estimate aerosol optical thickness by inverting the tabulated relationship:


$$\rho_{path}(865)_{|P} = \rho_{TOA}^{oz}(865) - t_{down}(865) * t_{up}(865)_{|P} * \rho_w(865) - T_{down}(865) * T_{up}(865) \rho_G \quad (26)$$

$$\rho_{path}(865)_{|P_{std}} \xrightarrow{LUT\ aer} \tau_a^{est}(865) \quad (27)$$

8. Keep only pixels consistent with the a priori known optical thickness:

$$|\tau_{865} - \tau_a^{est}(865)| \leq 0.02 \quad (28)$$

9. Eventually compute the glint intercalibration coefficient (relative to λ_{ref}) by:

	DIMITRI_v4.x ATBD Interband Vicarious Calibration over Sunlint	Reference: MO-SCI-ARG-TN-004c Revision: 2.1 Date: 30/09/2019 Page: 21
---	--	--

$$Ak(\lambda) = \frac{\rho_{TOA}^{OZ}(\lambda)}{\rho_{TOA}^{theo}(\lambda)} \quad (29)$$

In step 5.4, a first test must be to check that a solution does exist because the wind dependency of the Cox and Munk model is of the form:

$$CM54(w_m, \theta_s, \theta_v, \Delta\varphi) = \frac{A}{a+bw_m} e^{-\frac{B}{a+bw_m}} \quad (30)$$


With a and b being numerical constants (respectively 0.003 and 0.00512) and A and B coefficients depending on $(\theta_s, \theta_v, \Delta\varphi)$ only, the maximum is reached at $\overline{w_m} = (B - a)/b$; hence if $\rho_G > CM54(\overline{w_m}, \theta_s, \theta_v, \Delta\varphi)$ no solution can be found by the Newton algorithm (it would converge to $\overline{w_m}$ as an optimum but signal at λ_{ref} would not be consistent with the TOA modelling). In such a case, possibly corresponding to higher optical thickness than expected, pixels are discarded.

From step 6 it is important to include band $\lambda = \lambda_{ref}$ to check that $A(\lambda_{ref}) = 1$, meaning a perfect wind speed inversion.

When this procedure is launched pixel-by-pixel (by default for DIMITRI V4.x.y), the calibration coefficient of a given observation is computed as the median on all associated pixels (median is found to be more robust than a simple mean).

The main differences with this method compared to the Hagolle *et al.* (1999) method are:

- The marine model is updated from Morel (1988) to Morel and Maritorena (2001);
- An aerosol contribution is used at λ_{ref} , as it impacts transmittances, hence the glint and wind speed estimates. A final test eventually removes all points that do not fit with the a priori value τ_{865} . In practice this value can be chosen as the mean of AOT found by the Rayleigh method on the same oceanographic zones.
- The AOT inversion follows the very same approach as the operational ocean colour data processing (Antoine and Morel 1999);
- The modelling of the path atmospheric signal is made directly using the RTM simulations as a function of optical thickness;
- The downward and upward transmittances include the aerosol contribution.
- The pressure correction is applied following Bodhaine et al. 1999.
- The computing of Water Leaving reflectance takes in account the directional effects of BRDF.

	DIMITRI_v4.x ATBD Interband Vicarious Calibration over Sunlint	Reference: MO-SCI-ARG-TN-004c Revision: 2.1 Date: 30/09/2019 Page: 22
---	--	--

3 Uncertainty analysis

3.1 Published error budget

According to Hagolle *et al* (1999), the following are the main error sources for the methodology:

- Calibration error: error on the reference band induces error on the wind speed estimate. A 3% bias at 565nm introduces a 3% bias at 865 nm, hence no interband error. Error on 670 and 865 nm calibration would also impact aerosol detection, but this approach is not chosen in DIMITRI.
- Ozone: an uncertainty of 5% on ozone amount induces an error of less than 0.1%.
- Surface pressure: accurately known, it leads to 0.1%.
- Aerosol model: about 0.1%
- Chlorophyll: 0.3% error when the concentration is erroneous by 0.05 mg/m³ instead of 0.1 mg/m³; we understand it is implicitly for the 565 nm band, not in further red bands not impacted by chlorophyll in such oceanic regions.
- The total error due to statistical noise on the modelled atmospheric reflectance is around $\pm 0.4\%$

This leads to a total published uncertainty of better than 1% in interband calibration.


3.2 Sensitivity analysis on DIMITRI data

The main sources of uncertainty of the vicarious calibration are:

- The input parameters listed here above;
- The data screening condition, i.e. mainly clouds
- The pixel averaged on the calibration region.

Therefore a sensitivity analysis can be conducted with DIMITRI implementation to update the previously mentioned total error budget and to add new terms. We do not recompute uncertainty due to ozone and pressure as radiative transfer modellings are analogous between Hagolle *et al* (1999) and DIMITRI. Let us note that the published 0.1% uncertainty due to pressure is in line with our analysis and even an upper bound for calibrated bands close to the reference band (see Barker *et al* (2013) for details in the Rayleigh scattering methodology); we have also checked it directly by successively activating and de-activating the correction for pressure. In the following, the nominal run is a calibration of MERIS over SPG, with default options, in particular a MAR-99 aerosol model with 0.02 optical thickness at 865 nm (see section 4 for more details) and 665 nm as the reference band.

Sensitivity to cloud coverage: accepting 20% cloud coverage at ROI level, without considering pixel-by-pixel cloud mask, increases the number of calibration points from 10 to 15 and changes

	DIMITRI_v4.x ATBD Interband Vicarious Calibration over Sunlint	Reference: MO-SCI-ARG-TN-004c Revision: 2.1 Date: 30/09/2019 Page: 23
---	--	--

the median vicarious coefficients by 0.1% in the near-infrared bands; standard deviation of individual coefficients is unchanged. This is most probably due to similarity between glint and cloud signal at those bands (until 865 nm at least). We hence do not expect significant error when the 0% cloud coverage option is chosen, even if some clouds are not detected.

Sensitivity to aerosol optical thickness at 865 nm: changing the default value from 0.02 (assessed on SPG time-series in off-glint conditions) to 0.08 (Hagolle *et al.* 2004) impact the calibration of 0.1%, except at 885 nm where it is of 0.3%.

Sensitivity to chlorophyll: replacing the chlorophyll monthly climatology by its extreme values (0.04 and 0.08 mg/m³ over SPG) impacts the coefficients of 0.1%. This is a very good robustness compared to the Rayleigh vicarious calibration, obviously due to the considered bands in the red and near-infrared.

Sensitivity to sensor noise (pixel averaging): this can be assessed by comparing the DIMITRI output coefficient starting either from the averaged TOA signal, or from the pixel-by-pixel extraction (see section 3.3.3 about this processing mode). A first effect of using the averaged mode is to largely decrease the number of calibration points, from 10 to 3. The impact is around 0.1% or 0.2% depending on the bands.

Sensitivity to calibration of the reference band: we retrieve same number as Hagolle *et al.* (1999) until band 865 nm, i.e. a 3% calibration change roughly induces same change on the glint vicarious coefficients; the slight difference of 0.1% is added to the interband uncertainty. At 885 nm this discrepancy around the nominal 3% calibration is higher, of about 0.6%.

The total error budget is less than 0.6% from 681 to 865 nm and 1.3% at 885 nm due to extreme tests (coastal model at SPG), see Table 2. A maximum 1% uncertainty is assigned to all bands in DIMITRI interface. Because error on the input parameters can be considered as random (around true pressure, ozone, chlorophyll, etc.), this error budget contains mainly the random uncertainty, on punctual calibration points.

Table 2: Uncertainty budget of DIMITRI glint vicarious intercalibration coefficients in %, decomposed by sources. (*) comes from Hagolle *et al.* (1999)

Band	Ozone (*)	Pressure (*)	Aerosol model	AOT 865	Chl.	Pixel	Interband	Total
681	0.1	0.1	0	0.1	0.1	0.1	0.1	0.6
753		0.1	0.1	0.1	0.1	0.2	0.0	0.6
778		0.1	0.1	0	0.1	0.0	0.1	0.4
865		0.1	0	0.1	0.1	0.1	0.0	0.4
885		0.1	0.3	0.3	0.1	0.0	0.6	1.3

3.2.1 Tentative random/systematic uncertainty breakdown

Since vicarious calibration aims eventually at providing a unique set of coefficients, by averaging all targets, the uncertainty budget should rigorously be split into:

- The random uncertainty: its contribution to the averaged calibration coefficient goes down as more calibration points are considered
- The systematic uncertainty: its contribution remains the same whatever the number of points

No systematic source of error has been theoretically identified in previous uncertainty budget. Hence, we have tried to assess it experimentally, with real MERIS vicarious coefficients at SPG (most rigorous case study at present time due to knowledge of auxiliary data and proper radiative transfer LUT). Let us note σ the standard-deviation of a single target coefficient, i.e. the random uncertainty, and $\sigma(\overline{RA})$ the standard-deviation after averaging N targets; one has

$$\sigma(\overline{RA}) = \frac{\sigma}{\sqrt{N}} \quad (31)$$

Despite only few points are available (10), we observe that the experimental dispersion on \overline{RA} does not follow this shape when N varies from 2 to 10. Assuming that the observed dispersion can be understood as the mean square error (MSE), we have searched the bias and random uncertainty following this decomposition:

$$MSE(N) = Bias^2 + \left(\frac{\sigma}{\sqrt{N}}\right)^2 \quad (32)$$

In practice this is realised through a linear fit on $MSE(N) * N$. In order to avoid any statistical artefact when increasing the sample from $N=2$ to 10, we order it randomly and average over a large number of realisations (10 000).

Results of bias and σ are provided on Figure 7, and compared with previous sensitivity uncertainty budget. They remain very low, from 0.3% at 681 nm to 1.4% at 885 nm. Extrapolating these numbers on a large number of targets, i.e. decreasing at maximum the random contribution, results into a bias of less than 1%. This is very consistent with Hagolle *et al* (1999) estimates.

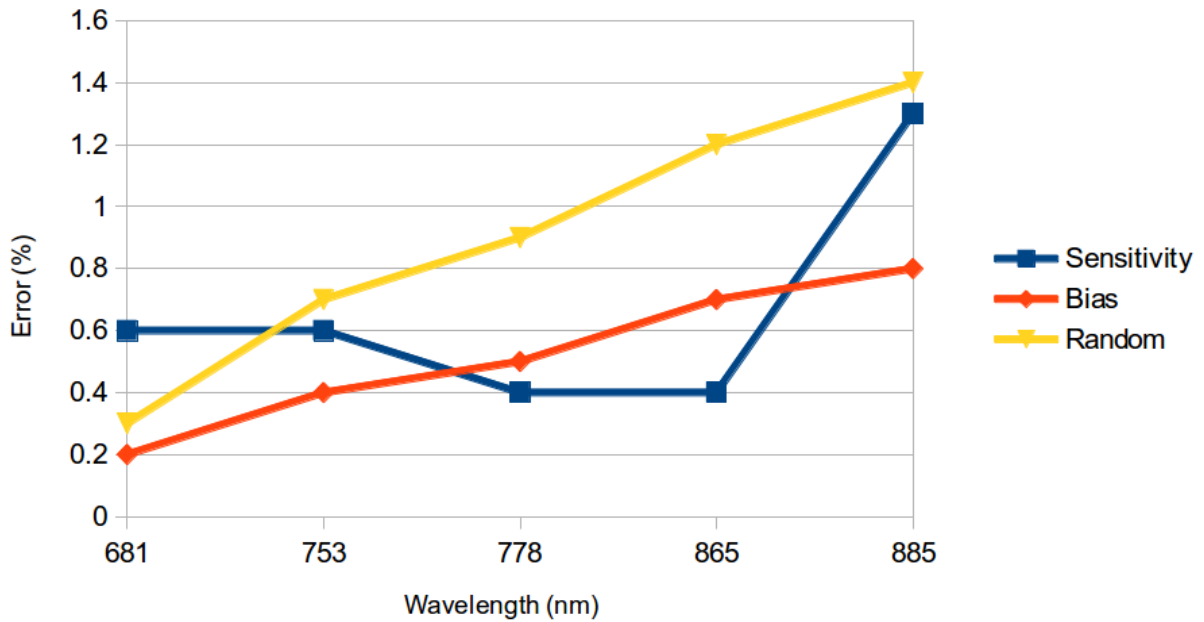


Figure 7 Tentative random (yellow)/bias(red) uncertainty breakdown of Sunlint vicarious method, based on MERIS vicarious coefficients at SPG. Blue uncertainty is from the sensitivity study of section 3.1.2

4 Presentation of the implementation in DIMITRI_v4.x making use of Hyperspectral LibradTran LUTs and Hydrolight version 5.2 mode

4.1 Radiative transfer Look up tables (LUT)

4.1.1 Format specification in DIMITRI

For every sensor (i.e. every set of wavelengths and spectral response), DIMITRI Rayleigh calibration needs one Rayleigh LUT and three other LUT for the aerosol optical thickness, downward total transmittance, upward total transmittance. This set of LUTs are generated automatically from a hyperspectral ones convoluted with the spectral response of the sensor under calibration. In order to compute the Water leaving reflectance, a LUT of the BRDF is included too.

All LUTs must be written in text file, with space as field separator, following the naming convention of

Table 3 to Table 7 below (AER may be any ASCII field identifying the aerosol model) and placed in directory AUX_DATA/RTM/SENSOR/. Any LUT satisfying this convention is detected by the GUI and can be used for the glint calibration. Reading and interpolation routines of DIMITRI_v4.x.y are based on header description, giving size and discretisation of the LUT; this allows totally generic sampling in the LUT. Only the wavelengths must follow those of the considered sensor as defined in the Bin/DIMITRI_Band_Names.txt configuration file (NaN or any field may be used if some bands are not processed in the RTM).

Table 3: RHOR_SENSOR.txt template for Rayleigh reflectance LUT (MERIS example)

```
# MERIS Rayleigh Reflectance
# lambda: 412.0000 443.0000 490.0000 510.0000 560.0000 620.0000 665.0000 681.0000
708.0000 754.0000 761.0000 779.0000 865.0000 885.0000 900.0000
# thetas: 0.0000 10.2229 21.3480 32.4790 43.6114 54.7444 65.8776 77.0110
# thetav: 0.0000 10.2229 21.3480 32.4790 43.6114 54.7444 65.8776 77.0110
# deltaphi: 0.0000 30.0000 60.0000 90.0000 120.0000 150.0000 180.0000
# wind: 0.5000 7.0000
# tau550: 0.0000 0.0400 0.0600 0.1300 0.3300
# Inner loop is on tau550, wind, then deltaphi, thetav, thetas, and bands
# Dimensions: 15 8 8 7 2 5
0.1254654675722122
...
```

Table 4: TAU_A_SENSOR_AER.txt template for spectral dependence of aerosol optical thickness LUT at given AER model (MERIS example for MAR-99)

```
# MERIS aerosol optical thickness for aerosol MAR99V
# Columns gives tau_a corresponding to 7 reference optical thickness at 550 nm, see DIMITRI ATBD
# Methodology for Vicarious Calibration
# (first optical thickness is zero)
# lambda: 412.0000 443.0000 490.0000 510.0000 560.0000 620.0000 665.0000 681.0000
708.0000 754.0000 761.0000 779.0000 865.0000 885.0000 900.0000
# Dimensions:      15      5
      0.000000000000000000  0.0511176362633705  0.0718025937676430  0.1442303806543350
0.3510798811912537
```

Table 5: TRA_DOWN_SENSOR_AER.txt template for downward total transmittance LUT at given AER model (MERIS example for MAR-99)

```
# MERIS total downward transmittance (direct+diffuse, Rayleigh+aerosol) for aerosol model
# MAR99V
# Columns gives t_up for 7 aerosol optical thickness (total, i.e. all layers) given in file
# TAU_A_MERIS.txt
# (first optical thickness is zero hence gives Rayleigh transmittance)
# lambda: 412.0000 443.0000 490.0000 510.0000 560.0000 620.0000 665.0000 681.0000
708.0000 754.0000 761.0000 779.0000 865.0000 885.0000 900.0000
# thetas: 0.0000 10.2229 21.3480 32.4790 43.6114 54.7444 65.8776 77.0110
# Inner loop is on tau550, thetas, then on bands
# Dimensions:      15      8      5
      0.8720846176147461  0.8649528622627258  0.8637801408767700  0.8601814508438110
0.8501554131507874
```

Table 6: TRA_UP_SENSOR_AER.txt template for upward total transmittance LUT at given AER model (PARASOL example for MAR-99)

```
# MERIS total upward transmittance (direct+diffuse, Rayleigh+aerosol) for aerosol model MAR99V
# Columns gives t_up for 7 aerosol optical thickness (total, i.e. all layers) given in file
# TAU_A_MERIS.txt
# (first optical thickness is zero hence gives Rayleigh transmittance)
# lambda: 412.0000 443.0000 490.0000 510.0000 560.0000 620.0000 665.0000 681.0000
```

```

708.0000 754.0000 761.0000 779.0000 865.0000 885.0000 900.0000
# thetav: 0.0000 10.2229 21.3480 32.4790 43.6114 54.7444 65.8776 77.0110
# Inner loop is on tau550, thetav, then on bands
# Dimensions:      15      8      5
      0.8720067739486694  0.8649499416351318  0.8637588024139404  0.8602198362350464
0.8503940701484680

```

Table 7: Structure of BRDF LUT for $L_w / E_d(0+)$, i.e. ρ_w/π .

```

# standard test file lut
labels val lambda theta_s theta_v delta_phi wind chl
units val_units nm deg deg deg ms-1 mgm-3
# dimensions
47 9 9 24 3 21
# lambda (nm)
340 350 360 370 380 390 400 410 420 430 440 450 460 470 480 490 500 510 520 530 540 550 560
570 580 590 600 610 620 630 640 650 660 670 680 690 700 710 720 730 740 750 760 770 780 790
800
# theta_s (deg)
0 10 20 30 40 50 60 70 80
# theta_v (deg)
0 10 20 30 40 50 60 70 80
# delta_phi (deg)
0 15 30 45 60 75 90 105 120 135 150 165 180 195 210 225 240 255 270 285 300 315 330 345
# wind (ms-1)
0.5 7 15
# chl (mgm-3)
0.01 0.02 0.03 0.04 0.05 0.06 0.08 0.09 0.1 0.11 0.12 0.2 0.3 0.5 1 2 3 4 5 10 20
# data, from inner loop to outer: lambda, theta_s, theta_v, delta_phi, wind, chl
0.0110553 0.0143791 0.0160343 0.0181537 0.0165921 0.0182862 0.0195017 0.0212603 0.0196469
0.0170696 0.0135635 0.0100285 0.00903388 0.0080296 0.00658734 0.0054679 0.00402303
0.00249237 0.00187594 0.00165135 0.00141281 0.0011099 0.000946941 0.000788989
0.000573875 0.000357569 0.000204086 0.000161111 0.000145257 0.000129044 0.000111461
9.82883e-05 7.69498e-05 6.78898e-05 6.06776e-05 5.17965e-05 4.06505e-05 2.90872e-05
1.85966e-05 1.20997e-05 8.7023e-06 7.98704e-06 7.39099e-06 7.15257e-06 7.27178e-06 7.62941e-
06 7.62941e-06

```


	DIMITRI_v4.x ATBD Interband Vicarious Calibration over Sunlint	Reference: MO-SCI-ARG-TN-004c Revision: 2.1 Date: 30/09/2019 Page: 29
---	--	--

Table 8: Structure of Rayleigh Optical thickness vs wavelength following Bodhaine et al., 1999.

# TAUR_BDHN99 AT LUT WAVELENGTH		
# Dimensions:	147	2
	2.5314788818359375	-0.1471159062290361

4.1.2 Atmospheric radiative transfer LUTs generation

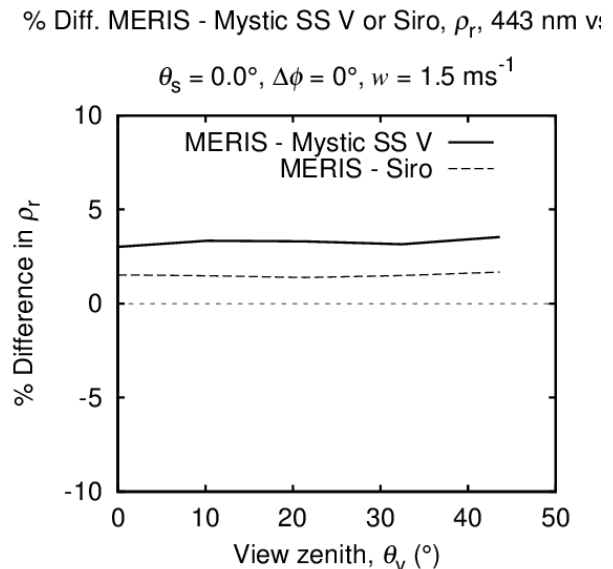
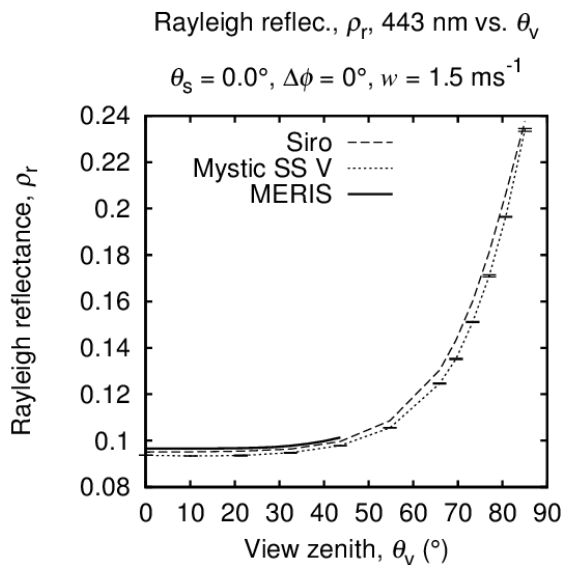
This section describes the generation of the look-up tables of atmospheric path reflectance, total transmission and relative optical thickness over wavelength as required by both the Rayleigh calibration and the sunlint calibration in DIMITRI. The look-up tables required are almost identical in structure to those used in the MERIS atmospheric correction scheme (Antoine and Morel 2011, Barker *et al.* 2012), but must be generated for every band of every sensor contained in DIMITRI. Currently these bands cover wavelengths from 340 nm to 5000 nm. While the Rayleigh correction requires wavelengths up to 700 nm, plus some in the NIR for aerosol detection, the glint calibration requires these tables at all wavelengths. Since many of the sensors in DIMITRI cover the same wavelength ranges the approach that has been taken is to produce one overall hyperspectral look-up table that can be convolved to each sensor band using the relative spectral response function (RSR) of each band. This approach makes the modelling more efficient and has the benefit that if new sensors are added to DIMITRI their Rayleigh and glint calibration look-up tables can be generated without further modelling, as long as the wavelengths are in the range 340 to 5000 nm.

4.1.3 Computational considerations

As the values required are for a Rayleigh scattering based calibration it is required to calculate them to the highest accuracy possible, which means they must be fully vectorial (with polarisation) since scalar modelling can introduce deviations of a few percentage in Rayleigh scattering (Hedley *et al.* 2013). Here, we have used a modified version of the LibRadtran Monte Carlo model Mystic (Mayer and Kylling 2005; Mayer 2009). This model is capable of vectorial or scalar modelling and the vectorial mode Rayleigh scattering has been validated against both the MERIS atmospheric correction look-up tables and an independent model, Siro, developed at the Finnish Meteorological Institute (Kujanpää 2013) (Figure 8).

The disadvantage of Mystic is that it is computationally slow, and being a Monte Carlo model is subject to statistical noise if insufficient computational effort is applied. In particular, with Mystic, each individual solar-view geometry requires a fully independent model run. Other models, such as the scalar Disort, can typically output results for a set of view zenith angles and relative

azimuths for each run, but with Mystic one run must be done for every combination of solar, view and relative azimuth angles. These computational considerations are not trivial and require some compromises to be made. On a standard workstation, to produce results with the statistical convergence shown in Figure 8 takes approximately 15 seconds per Mystic run on average (the run time increases with aerosol optical thickness). The MERIS atmospheric correction look-up tables are tabulated over 25 zenith angles, 23 azimuth angles, 3 wind speeds, 7 aerosol optical thicknesses. If tables were to be generated at this resolution at 400 wavelengths, for example, then the computation time would be $25 \times 25 \times 23 \times 3 \times 7 \times 400 \times 15$ seconds = 57 years. Therefore a compromise has been made in terms of the angular resolution of the modelling (Table 8). Modelling at every nanometre is unfeasible so 386 wavelengths from 340 – 5000 nm have been chosen as outlined in Table 8. This wavelength choice means that even the narrowest bands, MERIS at 9 nm, will have a minimum of two tabulated values within their RSR, but most will have many more. Conversely for bands that are wide this method ensures they are based on results spread across the band width. For the structure in Table 8, running the look-up table generation on a high-end workstation where calculation can be parallelised in up to 12 concurrent processes enables a look-up table for one aerosol model to be generated in approximately 4 weeks of compute time.



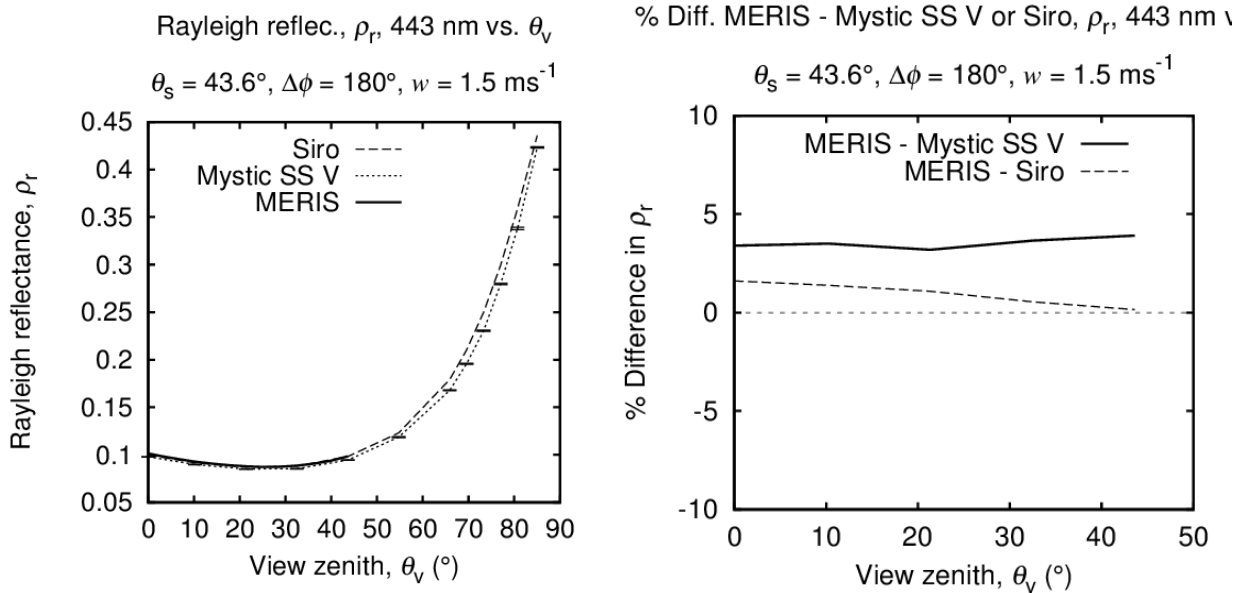


Figure 8: Example Rayleigh scattering results from Hedley *et al.* (2013) at 443 nm, from the MERIS atmospheric correction look-up tables and from Mystic and Siro in spherical shell vectorial mode. *Left side:* Rayleigh scattering with error bars showing ± 1 standard error on the mean for Mystic results. *Right side:* corresponding percentage difference between MERIS and Siro, and MERIS and Mystic. *Note:* both Mystic and Siro predict an error of only one third of a percent due to plane parallel versus spherical shell modelling at zero solar and zenith angles, hence this is not an explanation for the small deviations of 2 – 3% seen here.

4.1.4 Details of the required tables


The required tables are as follows:

1. Atmospheric path reflectance

This is calculated over a ‘black ocean’, i.e. the bottom boundary is a wind-blown air water interface but below surface reflection is zero. The direct reflectance path from the surface is excluded so that the reflectance represents photons that have undergone one or more atmospheric scattering events. To evaluate this requires a modification to the Mystic code to exclude photons that have not undergone an atmospheric scattering event. Note gaseous absorption is also excluded in this calculation as this is corrected for elsewhere..

2. Total transmission, upward and downward

The product of the total transmission upward and downward is evaluated from Mystic using another modification that excludes photons that have not reflected from the bottom boundary.

	DIMITRI_v4.x ATBD Interband Vicarious Calibration over Sunglint	Reference: MO-SCI-ARG-TN-004c Revision: 2.1 Date: 30/09/2019 Page: 32
---	---	--

The model is run over a Lambertian bottom of diffuse reflectance 0.1, the total transmittance is then the reflectance divided by 0.1 and corresponds to the assumption that water-leaving reflectance has a Lambertian BRDF. This assumption, while not strictly accurate (Morel and Gentili, 1993), will have minimal impact in this context. The assumption of Lambertian sub-surface reflectance has been shown to introduce only small errors (Yang and Gordon, 1997), see further discussion on this issue in Hedley *et al.* (2013). In addition the Lambertian assumption allows decoupling of the upward and downward transmittances, since the bottom boundary reflectance only has a dependence on the cosine of the solar zenith angle. The algorithm input requires that the upward and downward total transmittances be tabulated separately, although it is only their product that is used (Eqn. 22). If the model is run with a full set of solar zenith angles with view angle fixed (e.g. at zero) and vice versa the individual upward and downward transmissions could be calculated except there is unavoidably an unknown scaling factor between the upward and downward transmissions. In other words, for n zenith angles, there are $2n$ unknowns, but only $2n-1$ values to derive these from. This can be solved by assuming the upward and downward transmissions at zenith angle zero are equal. Note this is simply a trick to enable the algorithm implementation to be supplied with separate tables for upward and downward transmittance. When the product is formed the unknown factor disappears and the correct total transmission is used in Eqn. 22 regardless of this assumption.

This reflectance-based method for deriving the transmittance is required and appropriate because: 1) Mystic in general lacks outputs from which the total transmittances can be easily computed, and 2) it is the inverse of the process that must be captured, i.e. the reconstruction of the TOA reflectance from the bottom boundary reflectance (Eqn. 22). Decoupling of the water leaving reflectance from the atmospheric radiative transfer is equivalent to assuming that higher order photon interactions at the bottom boundary are negligible, i.e. that a photon reflects once only from the water body and hence the TOA reflectance is a linear function of the water body reflectance. This is valid, at least for diffuse reflectances up to 0.1, as shown in Figure 9 (see also Hedley *et al* 2013).

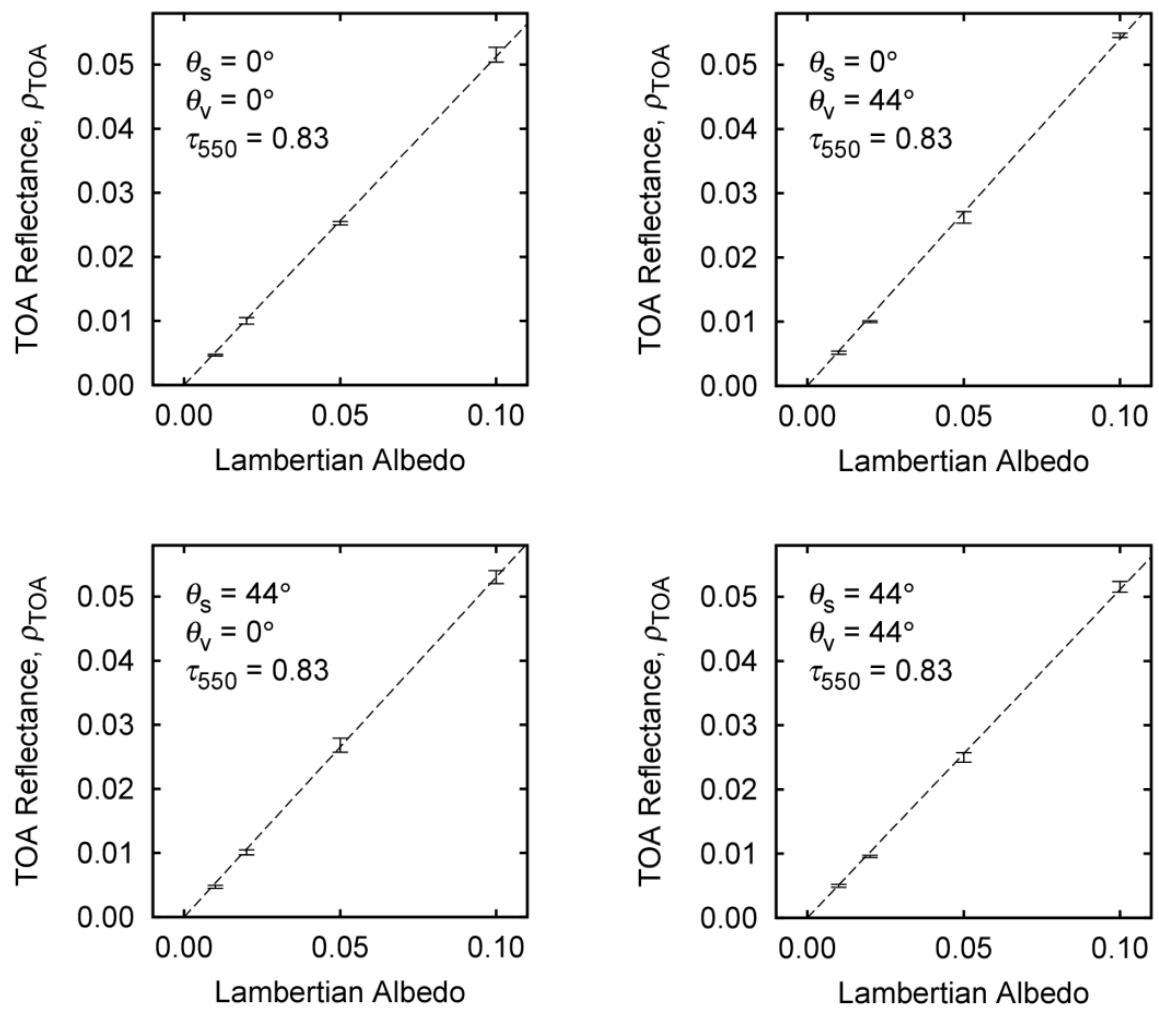


Figure 9: TOA reflectance from diffuse transmission paths as a function of bottom boundary Lambertian albedo from Hedley *et al.* (2013). These results were calculated in scalar spherical shell Mystic with the MAR-99 aerosol model (MERIS aerosol no. 4) $\tau_a(550) = 0.83$, but the general conclusion of linearity with bottom reflectance will hold for plane parallel vectorial modelling. Error bars are ± 1 standard error on the mean, line is least squares linear fit.

3. Variation in optical thickness with band

The radiative transfer models are run with aerosol models of differing specified optical thicknesses at wavelength 550 nm. The algorithms require that the corresponding aerosol optical thickness can be derived for other bands. This table enables that transformation to be made, for a given sensor and aerosol model it relates the optical thickness in one band to the others. These values are not dependent on solar-view geometry or wind speed. The values at each wavelength are output directly in the libRadtran run log at each wavelength. The values for each sensor band

are derived from the convolution by the sensor RSR.

4.1.5 Details of LibRadtran parameterisation

Certain details of the libRadtran parameterisation are listed below for reference. The next section describes the aerosol models.

- Standard US atmosphere ‘AFGLUS’
- Atmospheric height 120 km
- Pressure 1013 mb
- No gaseous absorption
- Plane parallel configuration
- Vectorial scattering
- For black ocean, vectorial Mischenko & Travis wind-blown sea surface including the correction introduced after libRadtran version 1.7

Mystic can also be run in spherical shell mode, and even for solar and zenith angles of zero this can make a third of a percentage difference in the Rayleigh scattering, and for other solar-view geometries the deviation can rise to several percent (Hedley *et al.* 2013). While the LUT generation code permits switching to spherical shell mode, within the context of this project the ‘traditional’ plane parallel assumption has been made.

Testing indicated that the Mystic options for forward or backward ray tracing and the ‘vroom’ optimisation did not reduce processing time or produce any overall improvement in statistical convergence. The ‘escape’ photon optimisation was enabled throughout.

Table 9: Structure of look-up tables for one aerosol model.

Parameter	Units	n	Values
λ	nm	147	340 to 1000 with step 10 (67), 1050 to 5000 step 50 (80)
θ_s	deg.	8	0, 10.2229, 21.3480, 32.4790, 43.6114, 54.7444, 65.8776, 77.0110
θ_v	deg.	8	0, 10.2229, 21.3480, 32.4790, 43.6114, 54.7444, 65.8776, 77.0110
$\Delta\phi$	deg.	7	0, 30, 60, 90, 120, 150, 180
wind	ms ⁻¹	2	0.5, 7
$\tau_a(550)$	-	5	0, 0.04, 0.06, 0.13, 0.33

total:	658560
--------	--------

Table 10: Components used in OPAC aerosol models as implemented in libRadtran (Hess *et al.* 1998)

Code	Meaning
inso	insoluble
waso	water_soluble
soot	soot
ssam	sea_salt_accumulation_mode
sscm	sea_salt_coarse_mode
minm	mineral_nucleation_mode
miam	mineral_accumulation_mode
micm	mineral_coarse_mode
mitr	mineral_transport
suso	sulfate_droplets

4.1.6 Aerosol models

Since generating a table for one aerosol model takes approximately 4 weeks of compute time, it has been restricted to only one aerosol model to the algorithm.

- **MAR99:** the MERIS atmospheric correction aerosol model no. 4

Details of the aerosol model parameterisations are given in the following two sections. Figure 10 shows aerosol optical thicknesses as a function of wavelength for different models, as output by LibRadtran, and indicates that MAR50 and MAR99 are correctly set-up as corresponding to the MERIS atmospheric correction LUT models. Interestingly although the OPAC model MC50 is described as corresponding to 50% relative humidity in the LibRadtran documentation, it corresponds closely to MAR99, which is considered as 99% relative humidity. However the slope of MC50 starts to deviate in the Near-Infra Red, so it is worthwhile to retain it in the algorithm. MAR50 and MAR99 represent the extreme slopes in optical thickness from the MERIS maritime aerosol models, so candidate models for future inclusion might be MAR70 and MAR90 which represent intermediate slopes.

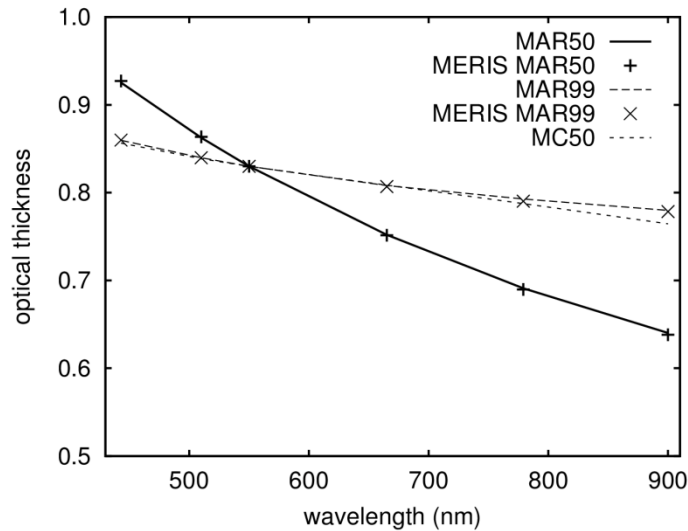


Figure 10: Aerosol optical thickness from 440 to 900 nm for the implemented aerosol models MAR50, MAR99 and MC50. Tabulated values for MAR50 and MAR99 from the MERIS atmospheric correction algorithm are also shown as point data.

MAR99, the MERIS atmospheric correction model

This model has been constructed for use in vectorial mode Mystic by use of the Mie scattering tool supplied with LibRadtran. The size distributions and refractive indices of the model components used are specified in the MERIS RMD and original paper by Shettle and Fenn (1979). The Mie tool is used to generate the wavelength dependent Mueller matrices and single scattering albedos, and these are conveniently output in netCDF files that LibRadtran takes as input. An additional input file specifies the vertical profiles of the differing aerosol components, which for these models occur in three distinct layers, 0 -2 km, 2 -12 km and 12 – 50 km. Again, the relative proportions were fixed according to the values in the MERIS RMD (Barker *et al.* 2012), but the 0 - 2 km fraction was scaled to reach the required $\tau_a(550)$ values as in Table 8. The models were validated by checking the relative optical thicknesses at different wavelengths to those tabulated in the MERIS RMD. Barring numerical differences in the modelling and undocumented details in the parameterisation, the MAR99 model should correspond exactly to hyperspectral versions of models 4 in the MERIS atmospheric correction.

4.2 Auxiliary data for marine modelling

Pure seawater absorption and scattering coefficients come from the NASA ocean color repository: http://oceancolor.gsfc.nasa.gov/DOCS/RSR/water_coef.txt.

The table of averaged cosine for downwelling reflectance (μ_d in Morel (1988) and Morel and Maritorena (2001)) comes from Morel *et al.* (2006) available on LOV repository at oceane.obs-vlfr.fr/pub/morel. Other parameters of the Morel and Maritorena (2001) model are directly taken from their table 2.

Refractive index of pure seawater comes from MERIS tables (Barker *et al.* 2012) and is spectrally interpolated for any wavelength.

As suggested by the sensitivity analysis, deriving meaningful coefficients needs the most realistic chlorophyll estimate. The ESA GlobColour project (<http://www.globcolour.info>) provides several ocean colour products derived from the merging of SeaWiFS, Aqua-MODIS and MERIS water leaving radiance data. The dataset covers the period 1998-2012. The dataset used in DIMITRI is the so-called Chl1-GSM product, at 0.25 degree spatial resolution. (Bouvet 2013). The merging of the three sensor data is done by minimizing the difference between the individual sensor water leaving radiances and the water leaving radiance predicted by a bio-optical model. The minimization process leads to the retrieval of the bio-optical model parameters, one of which is the chlorophyll-a concentration. The bio-optical model is the so-called GSM model (Maritorena *et al.* (2002) and Maritorena *et al.* (2005)). The monthly climatology Chl1 values averaged over the optimum regions of interest are computed (Bouvet 2013). . Note that users can still add any chlorophyll climatology file, which would be automatically processed by DIMITRI.

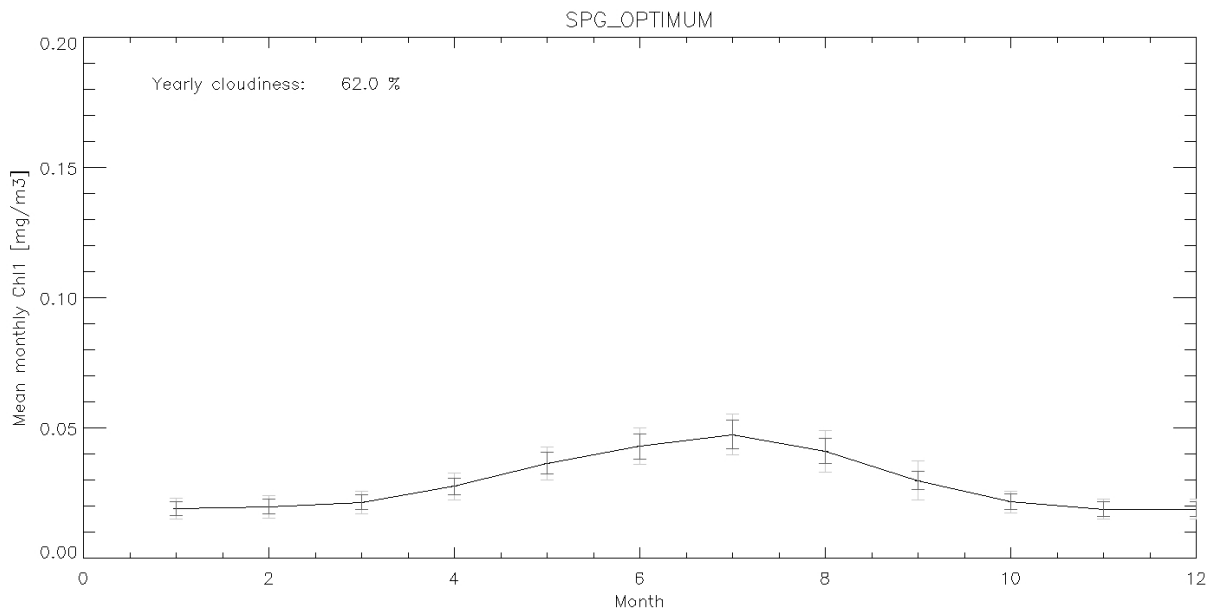



Figure 11 The monthly variations of the Chl1 climatology $CHL1_{clim}(month)$ derived from the full period 1998-2012 over SPG-optimum for applying the Raleigh scattering methodology. The black error bar is the associated uncertainty which the $CHL1_{uncertainty_{clim}}(month)$ and the grey error bar is the $CHL1_{stddev_{clim}}(month)$.

	DIMITRI_v4.x ATBD Interband Vicarious Calibration over Sunlint	Reference: MO-SCI-ARG-TN-004c Revision: 2.1 Date: 30/09/2019 Page: 38
---	--	--

4.3 Output files generated by the glint intercalibration

Five types of files are systematically generated for each glint vicarious calibration run:

1. **GLINT_CAL_LOG.txt:** log file summarising all options of the run (parameters).
2. **SITE_SENSOR_PROC_SUNGLINT_ARG_YYYYMMDD_hhmm.nc:** NetCDF file storing array REF_TO_SIM per band per pixel over the ROI
3. **SITE_SENSOR_PROC_SUNGLINT_ARG_YYYYMMDD-hhmm_DIR_BAND.JPG:** scatter-plot of the simulated reflectance to the observed one; and an histogram of the ratio observed-to-simulated one per band per acquisition.
4. **SITE_SENSOR_PROC_SUNGLINT_ARG_YYYYMMDD-hhmm_PERIOD.csv:** A csv format file storing the time-series of the calibration ratio over the analysed period.
5. **SITE_SENSOR_PROC_SUNGLINT_ARG_YYYYMMDD-hhmm_DIR_BAND_PERIOD.JPG:** A plot of the time-series of the ratios per direction per band over the analysed period.

4.4 DIMITRI modules/functions/architecture

The glint calibration methodology is implemented as an individual IDL module, called by a new GUI module (or directly in command line); it then calls several separated routines for specific jobs (e.g. computation of Rayleigh reflectance, of marine models, etc.).

Schematically, the main glint calibration module:


- Interfaces with the DIMITRI database to identify appropriate L1b extractions with respect to chosen region, sensor, processing version and year;
- Screens data for ROI cloud and region coverage pixel-by-pixel;
- Finds all pixels within other user defined parameters specific to the calibration method;
- Reads all RTM LUT;
- Performs the glint calibration band per band;
- Post-processed the coefficients (averaged, statistics);
- Outputs the individual and averaged calibration coefficients for each band in several text and image file, as defined in section 4.3.

4.5 HMI updates and User options

The glint calibration methodology allows both GUI and command line activation.

All processing parameters specific to the glint calibration are selectable by the user through a new window (Figure 12):

- Case study (region, sensor, processing version, year, output directory);
- Cloud and region coverage percentage; note that scenes having a manual cloud screening

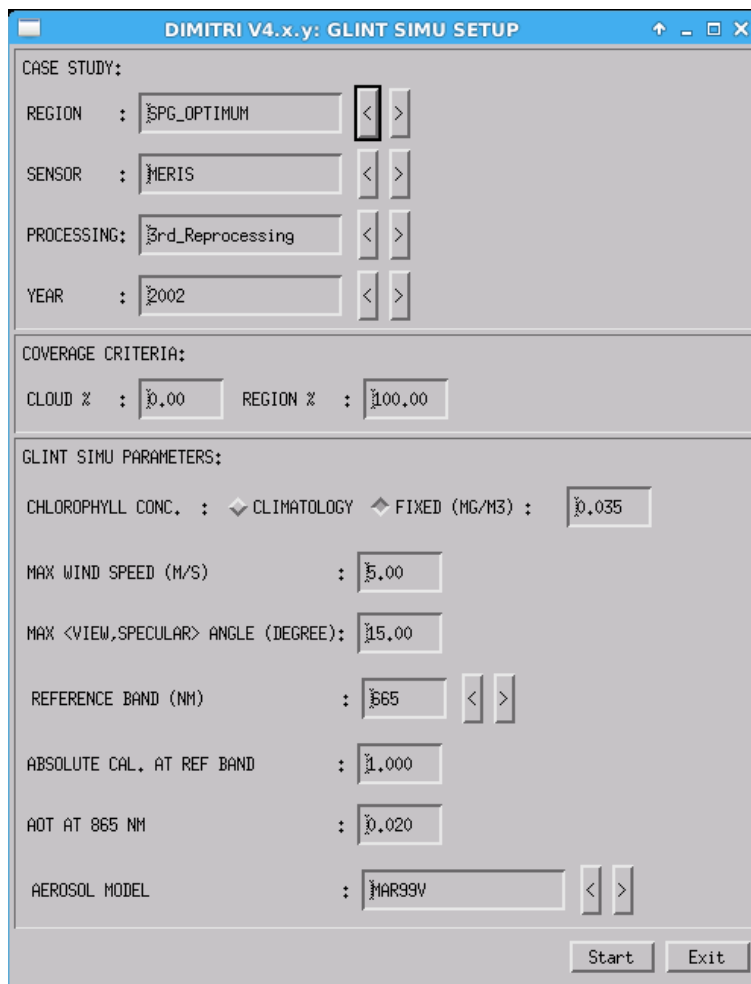
	DIMITRI_v4.x ATBD Interband Vicarious Calibration over Sunlint	Reference: MO-SCI-ARG-TN-004c Revision: 2.1 Date: 30/09/2019 Page: 39
---	--	--

set to 0 will be selected whatever the automated cloud screening value;

- Chlorophyll concentration, either by monthly climatology put in the DIMITRI auxiliary folder or by a fixed values;
- Maximum wind speed;
- Maximum angle between viewing and specular directions;
- Reference band for the calibration;
- Absolute calibration coefficient for the reference band; this coefficient must be understood as in the Rayleigh absolute calibration (RAk, see Alhammoud and Hedley 2019), i.e.

$$\rho_{TOA}^{cal}(\lambda_{ref}) = \rho_{TOA}^{obs}(\lambda_{ref}) * RAk(\lambda_{ref}) \quad (33)$$

- Aerosol optical thickness at 865 nm;
- Aerosol model, among an automated list built on all models existing in DIMITRI auxiliary folder, sensor per sensor.



DIMITRI V4.x.y: GLINT SIMU SETUP

CASE STUDY:

REGION : SPG_OPTIMUM < >

SENSOR : MERIS < >

PROCESSING: 3rd_Reprocessing < >

YEAR : 2002 < >

COVERAGE CRITERIA:

CLOUD % : 0.00 REGION % : 100.00

GLINT SIMU PARAMETERS:

CHLOROPHYLL CONC. : CLIMATOLOGY FIXED (MG/M3) : 0.035

MAX WIND SPEED (M/S) : 5.00

MAX <VIEW,SPECULAR> ANGLE (DEGREE): 15.00

REFERENCE BAND (NM) : 665 < >

ABSOLUTE CAL. AT REF BAND : 1.000

AOT AT 865 NM : 0.020

AEROSOL MODEL : MAR99V < >

Start Exit

Figure 12: DIMITRI v4.x.y window for parameterising the glint vicarious calibration

5 Results and implementation comparisons

Note: Wind speed modulus and gas concentrations used for atmospheric quantities computation come from DIMITRI auxiliary data associated to each measurement, as stored in **SITE_SENSOR_PROC_SUNGLINT_ARG_YYYYMMDD_hhmm.nc** files. The default values of $w_m=5\text{m/s}$ and $O_3=300\text{ DU}$ are automatically selected in order to present results for all sensors.

In all following results default options of the glint calibration are used, unless specified:

- 0% ROI cloud coverage,
- 100% ROI coverage,
- Maximum wind modulus of 5 m/s,
- Maximum angle between viewing and specular direction of 15°,
- Reference band chosen at 665 nm,
- Aerosol optical thickness at 865 nm of 0.02 and MAR-99 aerosol model.

The chlorophyll concentration comes from previously detailed climatology.

5.1 DIMITRI implementation results for MERIS

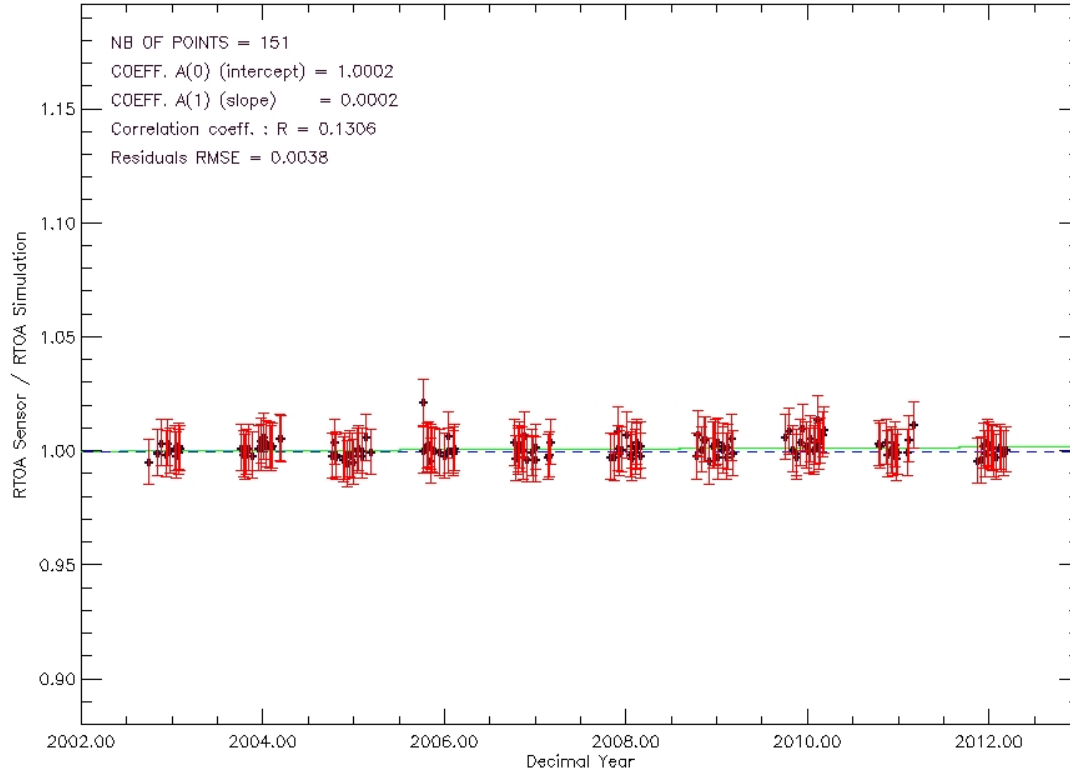
The time-series statistics over SPG for MERIS 3rd reprocessing are detailed in Table 11 and the calibration ratios are plotted on Figure 13, taking an absolute calibration coefficient at 665 nm of 0.977, as found with Rayleigh scattering calibration (see Alhammoud and Hedley 2019). Coefficients present a slight linear spectral variation, except at 885 nm, and values variation is within 2% from 681 nm to 885 nm wrt to band 7 (665 nm). Being outside the estimated 2% error budget of the on-board L1b calibration (Bourg and Delwart, 2012) for red bands is directly due to the choice of calibration coefficient at reference band 665 nm, hence to the Rayleigh scattering result. The standard-deviation is relatively weak (0.5% max at 885 nm), compared for instance to the DIMITRI Rayleigh calibration and largely within the mean uncertainty (1%). This can be also seen on the time-series plots (Figure 13), showing a perfect alignment of all coefficients from 2002 to 2012.

Table 11: MERIS 3rd reprocessing glint intercalibration coefficients over SPG, relative to 665 nm (AR_{665} : 0.977)

Band (nm)	Median Ak	Standard-deviation	Mean uncertainty	N
665.00	0.977	0	0.01	151
681.00	0.979	0.001	0.01	151
753.00	0.971	0.002	0.01	151
778.00	0.967	0.003	0.01	151

865.00	0.963	0.005	0.01	151
885.00	0.952	0.005	0.01	151

SUNGLINT_ARG – RTOA Sensor vs RTOA Simulation Temporal Variability – PERIOD [2002–2013]
SPG_OPTIMUM_MERIS_3rd_Reprocessing_SUNGLINT_ARG_20181115–1326_DIR01_BAND (06 – 620nm)



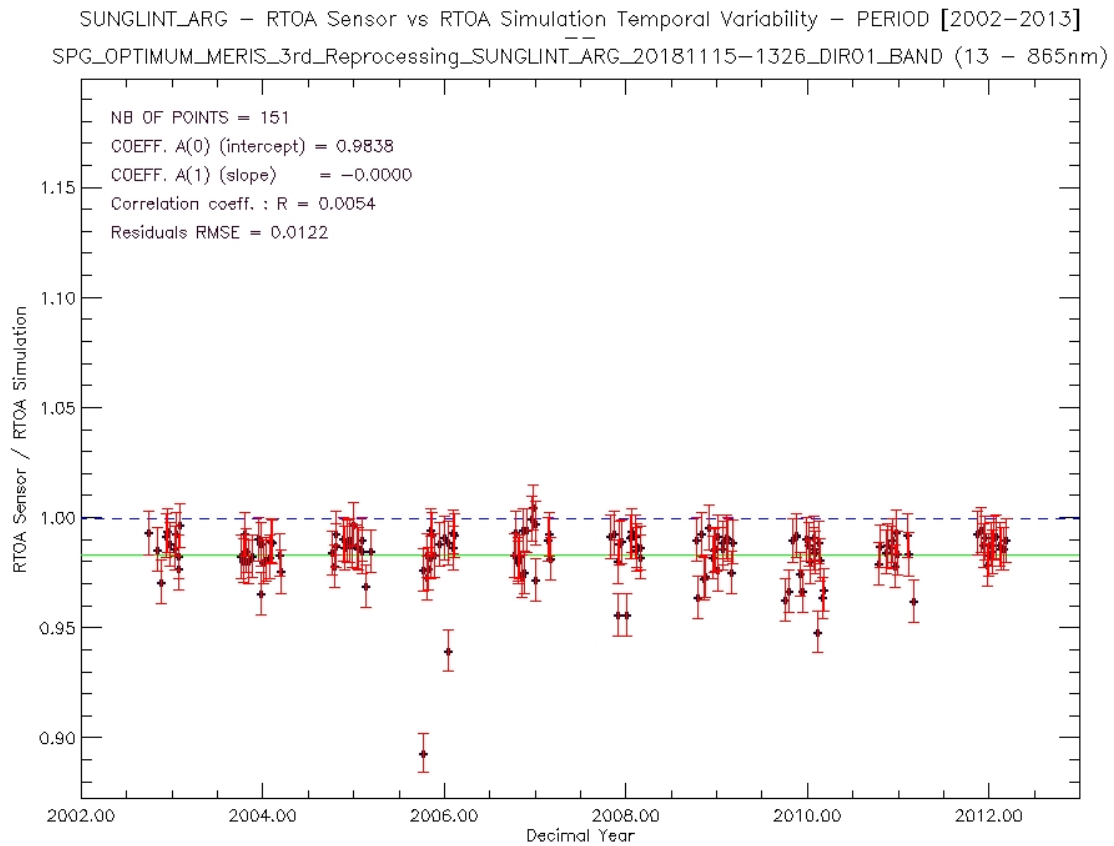



Figure 13: Time-series of (top) band-6 and (bottom) band-13 from MERIS 3rd reprocessing glint intercalibration coefficients as ratios TOA-Sensor/TOA-Simulation (665 nm as reference) over SPG-OPTIMUM, Error bars are method's uncertainty .

The coefficients are very comparable at SIO, see Table 12 and Figure 13.

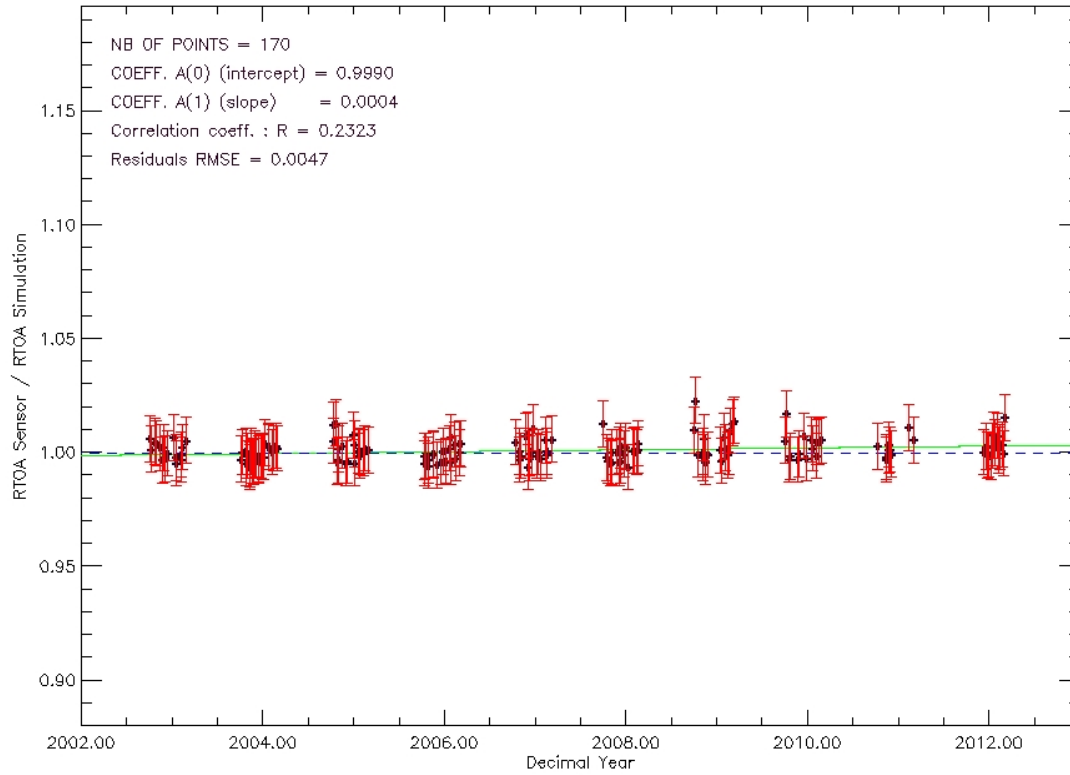
Table 12: MERIS 3rd reprocessing glint intercalibration coefficients over SIO-Optimum, relative to 665 nm

Band (nm)	Median Ak	Standard-deviation	Mean uncertainty	N
665.00	0.987	0	0.01	171
681.00	0.989	0.002	0.01	171
753.00	0.981	0.002	0.01	171
778.00	0.977	0.003	0.01	171
865.00	0.973	0.005	0.01	171

	<p style="text-align: center;">DIMITRI_v4.x ATBD Interband Vicarious Calibration over Sunlint</p>	<p>Reference: MO-SCI-ARG-TN-004c Revision: 2.1 Date: 30/09/2019 Page: 44</p>
---	--	--

885.00	0.963	0.005	0.01	171
--------	-------	-------	------	-----

SUNGLINT_ARG – RTOA Sensor vs RTOA Simulation Temporal Variability – PERIOD [2002–2013]
SIO_OPTIMUM_MERIS_3rd_Reprocessing_SUNGLINT_ARG_20181109–1419_DIR01_BAND (06 – 620nm)



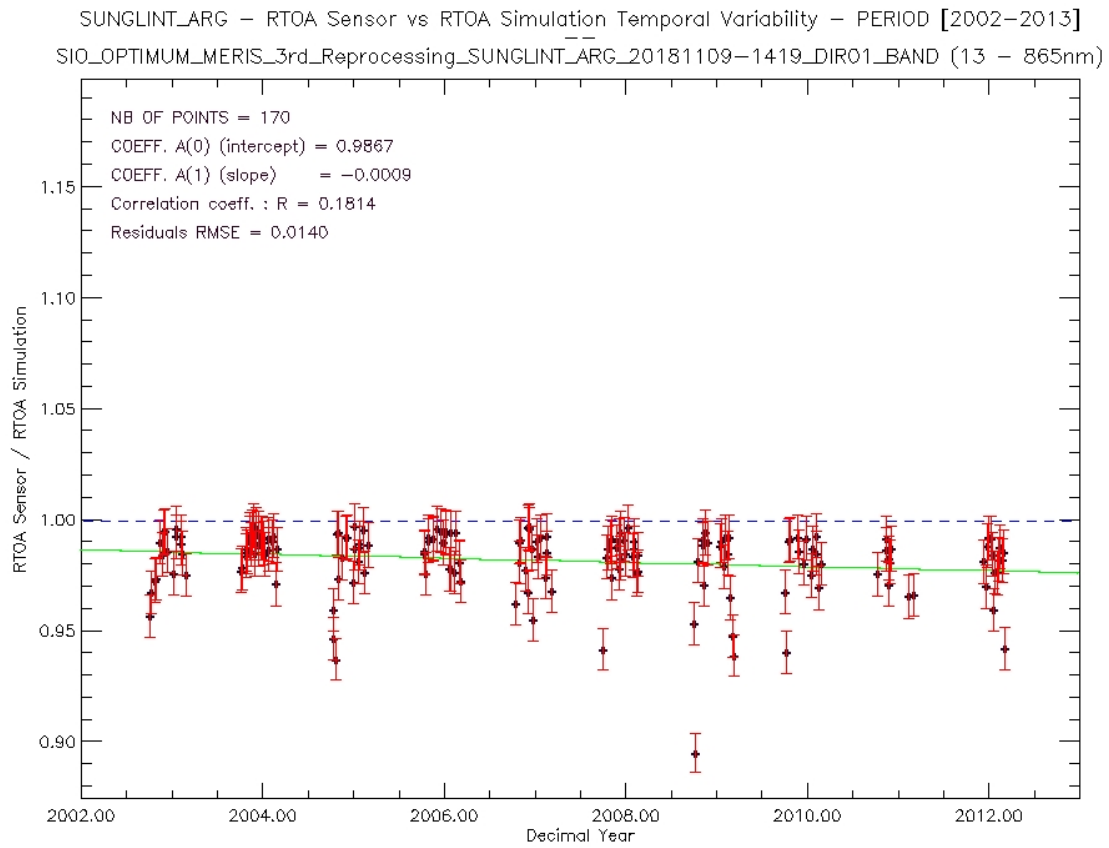


Figure 14: Time-series of (top) band-6 and (bottom) band-13 from MERIS 3rd reprocessing glint intercalibration coefficients as ratios TOA-Sensor/TOA-Simulation (665 nm as reference) over SPG-OPTIMUM, Error bars are method's uncertainty

5.2 DIMITRI implementation results for other sensors

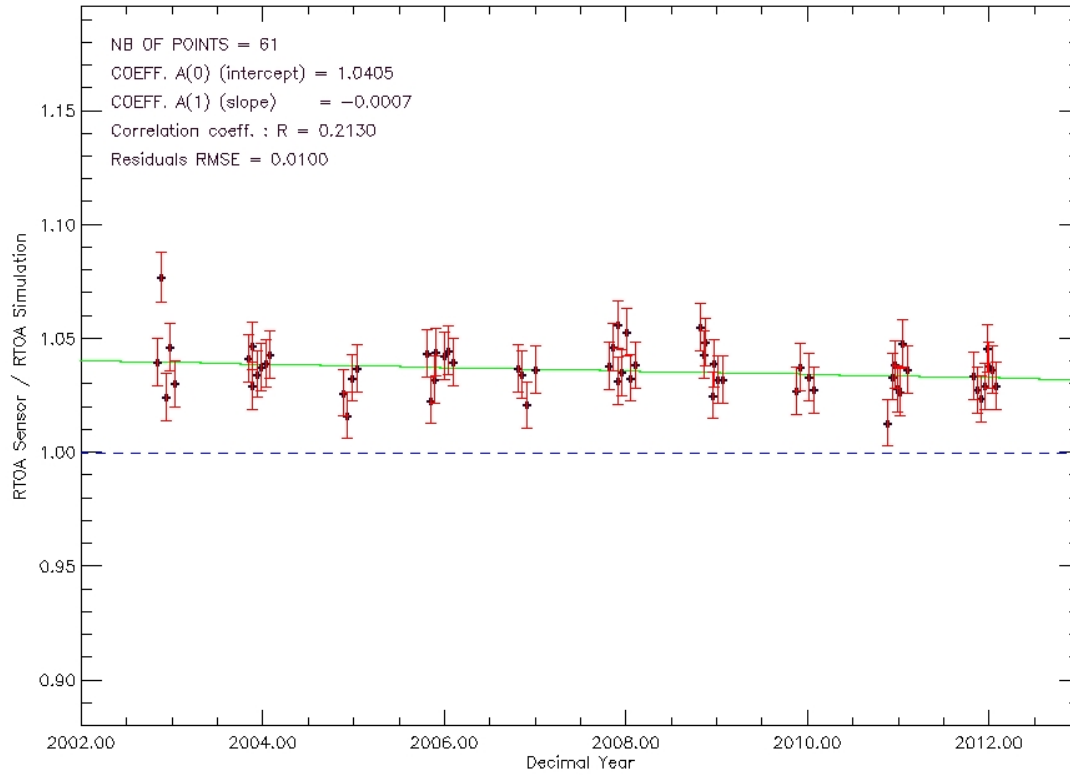
Glint intercalibration coefficients over SPG for AATSR are depicted in Table 13 and the time-series are displayed on Figure 15.

We use the Rayleigh vicarious coefficient at the reference band, $RAk(666)=0.997$ (median value). For this sensor, the near-infrared relative gain at 865 nm is consistent with Fougnie *et al* (2012) despite difference in Rayleigh absolute coefficients.

Table 13: AATSR 3rd reprocessing glint intercalibration coefficients over SPG, relative to 666 nm

Band (nm)	Median Ak	Standard-deviation	Mean uncertainty	N
555.00	1.033	0.002	0.01	61
666.00	0.997	0.0	0.01	61
865.00	0.987	0.005	0.01	61

SUNGLINT_ARG – RTOA Sensor vs RTOA Simulation Temporal Variability – PERIOD [2002–2013]
SPG_OPTIMUM_AATSR_3rd_Reprocessing_SUNGLINT_ARG_20190317–1723_DIR01_BAND (01 – 555nm)



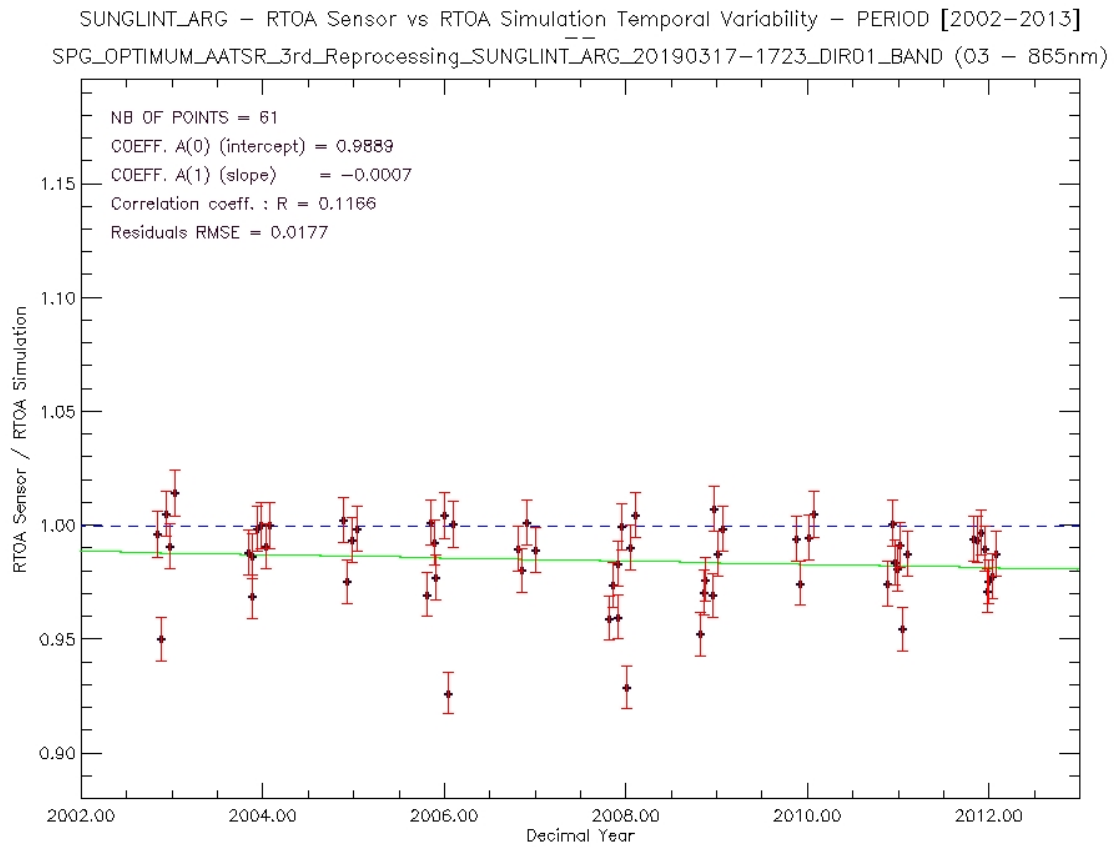



Figure 15: Time-series of (top) band-1 and (bottom) band-3 from AATSR 3rd reprocessing glint intercalibration coefficients as ratios TOA-Sensor/TOA-Simulation (666 nm as reference) over SPG-OPTIMUM, Error bars are method's uncertainty.

	DIMITRI_v4.x ATBD Interband Vicarious Calibration over Sunlint	Reference: MO-SCI-ARG-TN-004c Revision: 2.1 Date: 30/09/2019 Page: 50
---	--	--

6 Discussion and conclusion

The glint calibration method implemented in DIMITRI_v3.0 follows essentially the initial work of Hagolle *et al.* (1999), with several adaptations taking into account more recent and well-validated ocean colour modelling in marine reflectance and aerosol contribution. A noticeable difference is that the aerosol optical thickness cannot be computed from simultaneous off-glint observations and is therefore fixed for once and all. It is a similar solution as in Hagolle *et al.* (2004) for VEGETATION.


Several improvements have been carried out on the Interband sunlint calibration method in the current DIMITRI v4.x.y version such as:

- Implementing a new hyperspectral LUTs for the aerosol and atmospheric reflectance.
- Implementing the atmospheric pressure adjustment following Bodhaine et al. 1999.
- Implementing hyperspectral LUTs of the water leaving reflectance taking in account the BRDF effects.

The DIMITRI_v4.x.y HMI allows users to easily choose all main parameters of the calibration (thresholds, chlorophyll concentration, aerosol model, etc.). Automated handling of auxiliary files also gives users the possibility to immediately test other parameterisations of the signal modelling, both for the marine contribution, e.g. chlorophyll climatology, coefficients of the Morel and Maritorena (2011) model and atmospheric component (e.g. new look-up tables with different geometrical discretisation or aerosol models).


Vicarious coefficients presented here for MERIS are a slightly lower than the 2% expected L1b calibration uncertainty (Bourg and Delwart, 2012), but this is relative to the 2.6% calibration factor of reference band coming from Rayleigh scattering methodology. Taking a 0% factor at 665 nm produces a set of coefficients very close to unity from 681 to 885nm. This shows the importance of ensuring a perfect calibration at reference band. Also taking into account water vapour absorption would probably improve the results in the NIR bands.

It appears that the glint coefficients in the red and near-infrared are extremely stable along the years (very low standard-deviation), contrary to the Rayleigh vicarious calibration in the visible. This probably comes from the very strong and well-modelled glint signal at the reference band, contrary to the off-glint marine signal in the visible bands highly sensitive to the chlorophyll content.


	DIMITRI_v4.x ATBD Interband Vicarious Calibration over Sunlint	Reference: MO-SCI-ARG-TN-004c Revision: 2.1 Date: 30/09/2019 Page: 51
---	--	--

7 References


- Alhammoud, B., Hedley, J. (2019) Rayleigh scattering methodology for vicarious calibration, DIMITRI ATBD ref. ARG_DIM_QA4EO -TN-004b, Issue 2.1
- Antoine, D. and A. Morel (1999). A multiple scattering algorithm for atmospheric correction of remotely-sensed ocean colour (MERIS instrument): principle and implementation for atmospheres carrying various aerosols including absorbing ones, IJRS, 20, 1875-1916.
- Antoine, D. and Morel, A. (2011). MERIS ATBD 2.7 Atmospheric Correction of the MERIS observations Over Ocean Case 1 waters. Technical Report MERIS ATBD 2.7 v5.1-July2011 (Version 5.1).
- Barker, K., Marrable, D., Hedley, J., Mazeran, C. (2013) Rayleigh scattering methodology for vicarious calibration, DIMITRI ATBD ref. MO-SCI-ARG-TN-004b, Issue 1.0
- Barker, K., Antoine, D., Bourg, L., Brockmann, C., Doerffer, R., Fischer, J., Moore, G., Santer, R., and Zagolski, F. (2012). Reference Model for MERIS Level 2 Processing. Third MERIS reprocessing: Ocean Branch. Technical Report PO-TN-MEL-GS-0026 (Version 5.2)
- Bourg, L. and S. Delwart (2012) MERIS instrument calibration. Available at <http://earth.eo.esa.int/pcs/envisat/meris/documentation/>
- Bouvet, M. (2006). Intercomparisons of imaging spectrometers over the Salar de Uyuni (Bolivia). *Proc. 2nd MERIS and AATSR Calibration and Geophysical Validation Meeting (MAVT-2006)*, 20-24 March 2006, ESRIN.
- Bouvet, M. (2011). Simulation of VEGETATION measurements with DIMITRI. ESA Tech. Note: TEC-EEP/2011.713/MB
- Bouvet, M. (2013) Selection of optimum oceanic sites for applying the Rayleigh scattering methodology to optical space sensors. ESA Technical Note, 06/12/2013.
- Bouvet M., Goryl P., Chander G. Santer R., and Saunier S. 2007. Preliminary radiometric calibration assessment of ALOS AVNIR-2. Proc. Geoscience and Remote Sensing Symposium, IGARSS 2007
- Cox, C., and W. Munk (1954), Statistics Of The Sea Surface Derived From Sun Glitter, J. Mar. Res., 13, 198 – 227
- Fougnie, B., Patrice Henry, P., Morel, A., Antoine, D., Montagner, F. (2002). Identification and characterization of stable homogenous oceanic zones: climatology and impact on in-flight calibration of space sensors over rayleigh scattering. Ocean Optics XVI, Santa Fe, NM.
- Fougnie, B., Bracco, G., Lafrance, B., Ruffel, C., Hagolle, O., Tinel, C. (2007) PARASOL in-flight calibration and performance, Applied Optics, Vol. 46, No 22, 5435-5451

	DIMITRI_v4.x ATBD Interband Vicarious Calibration over Sunlint	Reference: MO-SCI-ARG-TN-004c Revision: 2.1 Date: 30/09/2019 Page: 52
---	--	--

- Fougnie, B., Henry, P., Lachérade, S., and P. Gamet (2012) Radiometric calibration of desert sites and oceanic target. Sentienl-3 calibration and validation planning meeting, ESA/ESRIN, March 2012.
- Hagolle *et al.* (1999) Results of POLDER in-flight Calibration, IEEE Transactions on Geoscience and Remote Sensing, May 1999, Volume 37, Number 03
- Hagolle, O., JM. Nicolas, B. Fougnie, F. Cabot, P. Henry. 2004. "Absolute Calibration of VEGETATION Derived From an Interband Method Based on the Sun Glint Over Ocean", IEEE Transactions On Geoscience And Remote Sensing, Vol. 42, No. 7
- Hansen, J.E. and L. Travis, 1974. Light scattering in planetary atmospheres, Space Science Reviews, 16: 527-610.
- Hedley (2017), QA4EO DIMITRI Evolution LUT description and use, Ref: ARG_DIM_QA4EO_LUT_SUM, 8th, Feb. 2017.
- Hedley (2018), Pressure, latitude and CO2 adjustments, Ref: ARG_DIM_QA4EO_ATM, 18 Jan. 2018.
- Hedley (2019), Water-leaving reflectance BRDF, Ref: ARG_DIM_QA4EO_WL_BRDF, 26th Feb. 2019.
- Hedley J, Lamquin N, Mazeran C. (2013) Atmospheric Correction for Ocean Colour in a Spherical Shell Atmosphere. Algorithm Theoretical Basis Document. ESA Report GEOHR-D6 AO/1-7084/12/NL/AF (Version 0.9.2).
- Hess M, Koepke P, Schult I (1998) Optical Properties of Aerosols and Clouds: The software package OPAC. Bulletin of the American Meteorological Society 79(5) 831-844.
- Kay, S., Hedley, J., Lavender, S., and Nimmo-Smith, A. (2011). Light transfer at the ocean surfacemodelled using high resolution sea surface realizations. Opt. Express, 19(7):6493–6504.
- Kirk JTO (1981) A Monte-Carlo study of the nature of the underwater light field in, and relationships between optical properties of, turbid yellow waters, Aust. J. Mar. Freshwater Res., 32, 517-532.
- Kou, L., D. Labrie, P. Chylek, 1993, "Refractive indices of water and ice in the 0.65-2.5 m spectral range," Appl. Opt.,32, 3531-3540 (1993).
- Kujanpää, J. (2013). Atmospheric Correction for Geostationary High Resolution Ocean Applications (GEO-HR). Forward Model Description. Technical Report ESA Report GEOHR-D2 AO/1-7084/12/NL/AF (Version 1.1).
- Lerebourg, C., Mazeran, C., Huot, J-P., Antoine, A. (2011) Vicarious adjustment of the MERIS Ocean Colour Radiometry. MERIS ATBD 2.24, Issue 1.0
- Mayer, B. (2009). Radiative transfer in the cloudy atmosphere. EPJ Web of Conferences, 1:75–99.

	DIMITRI_v4.x ATBD Interband Vicarious Calibration over Sunlint	Reference: MO-SCI-ARG-TN-004c Revision: 2.1 Date: 30/09/2019 Page: 53
---	--	--

- Mayer, B. and Kylling, A. (2005). Technical note: The libradtran software package for radiative transfer calculations - description and examples of use. *Atmospheric Chemistry and Physics*, 7:1855–1877.
- MERIS Level 2 Detailed Processing Model, June 2011, ref. PO-TN-MEL-GS-0006, Issue 8.0B available at <http://earth.eo.esa.int/pcs/envisat/meris/documentation>
- M. I. Mishchenko and L. D. Travis, Satellite retrieval of aerosol properties over the ocean using polarization as well as intensity of reflected sunlight. *J. Geophys. Res.* 102, 16989-17013 (1997).
- Mobley CD, Sundman L (2013) Hydrolight 5.2 User's Guide. Sequoia Scientific. Available online: <http://www.sequoiasci.com/products/Hydrolight.aspx>
- Mobley CD, Gentili B, Gordon HR, Jin Z, Kattawar GW, Morel A, Reinersman P, Stamnes K, Stavn RH (1993) Comparison of numerical models for computing underwater light fields. *Applied Optics* 32(36), 7484-7504.
- Morel, A. (1988). Optical modeling of the upper ocean in relation to its biogenous matter content (case 1 water), *Journal of Geophysical Research*, 93, 10,749-10,768.
- Morel, A., and S. Maritorena (2001). Bio-optical properties of oceanic waters: A reappraisal. *Journal of Geophysical research*, 106, 7763-7780
- Morel, A., and B. Gentili (1996). Diffuse reflectance of oceanic waters. 3. Implication of bidirectionality for the remote-sensing problem. *Applied Optics*, 35, 4850-4862.
- Morel, A. and Gentili, B. (1993). Diffuse reflectance of oceanic waters. ii bidirectional aspects. *Applied Optics*, 32(33):6864–6879.
- Morel, A., Gentili, B., Chami, M., and J. Ras (2006) Bio-optical properties of high chlorophyll Case1 waters and of yellow-substance-dominated Case2 waters. *Deep-Sea Res. I*, 53, 1439-1559
- Nicolas, J.-M., Deschamps, P.-Y., & Hagolle, O., 2006. Radiometric Calibration of the Visible and Near-Infrared Bands of Seviri Using Rayleigh Scattering and Sun-Glint Over Oceans, *Proceedings of the 3rd MSG RAO Workshop (ESA SP-619)*. 15 June 2006, Helsinki, Finland. Editor: D. Danessy, p.19
- Pope, R. M. and E. S. Fry, 1997, "Absorption spectrum (380-700 nm) of pure water. II. Integrating cavity measurements," *Appl. Opt.*, 36, 8710-8723.
- Shettle, E.P. and R.W. Fenn, 1979. Models for the aerosols of the lower atmosphere and the effects of humidity variations on their optical properties. *Environmental Research Papers*, AFGL-TR-79-0214, 20 September 1979, AFGL, Hanscom (Mass.).
- Smith, R.C. and K.S. Baker, 1981, "Optical properties of the clearest natural waters (200-800 nm)," *Appl. Opt.*, 20, 177-184.


	DIMITRI_v4.x ATBD Interband Vicarious Calibration over Sunlint	Reference: MO-SCI-ARG-TN-004c Revision: 2.1 Date: 30/09/2019 Page: 54
---	--	--

Vermote, E., R. Santer, P.Y. Deschamps and M. Herman, In-flight Calibration of Large Field-of-View Sensors at Short Wavelengths using Rayleigh Scattering, Int. Journal of Remote Sensing, 13, No 18, 1992. <http://www.tandf.co.uk/journals/tres>

Yang, H. and Gordon, H. R. (1997). Remote sensing of ocean color: assessment of water-leaving radiance bidirectional effects on atmospheric diffuse transmittance. Applied Optics, 36(30):7887–7897.

Zagolski, F. (2010) Specification of the Contents of the MERIS Radiative Transfer Tools used to Generate the Level-2 Auxiliary Data Products. Doc PO-RS-PAR-GS-0003, issue 4.A

Závody, A. M., P. D. Watts, D. L. Smith, C. T. Mutlow, 1998. A Novel Method for Calibrating the ATSR-2 1.6- μm Channel Using Simultaneous Measurements Made in the 3.7- μm Channel in Sun Glint. J. Atmos. Oceanic Technol., 15, 1243–1252.

	<p style="text-align: center;">DIMITRI_v4.x ATBD Interband Vicarious Calibration over Sunlint</p>	<p>Reference: MO-SCI-ARG-TN-004c Revision: 2.1 Date: 30/09/2019 Page: 55</p>
---	--	--

[End of Document]